1 # A Regional multi-Air Pollutant Assimilation System (RAPAS v1.0)

2 # for emission estimates: system development and application

3 Shuzhuang Feng[1], Fei Jiang[1,2], Zheng Wu[3], Hengmao Wang[1,2], Wei He[1], Yang Shen[1],

4 Lingyu Zhang[1], Yanhua Zheng[1], Chenxi Lou[1], Ziqiang Jiang[4], Weimin Ju[1,2]

5

6 [1] *Jiangsu Provincial Key Laboratory of Geographic Information Science and Technology, International*

7 *Institute for Earth System Science, Nanjing University, Nanjing, 210023, China*

8 [2] *Jiangsu Center for Collaborative Innovation in Geographical Information Resource Development and*

9 *Application, Nanjing, 210023, China*

10 [3] *Chongqing Institute of Meteorological Sciences, Chongqing, 401147, China*

11 [4] *Jiangsu Environmental Monitoring Center, Nanjing, 210019, China*

12
13
14
15

16 *Correspondence to*: Fei Jiang (jiangf@nju.edu.cn)

17
18
19
20
21
22
23
24
25
26
27
28
29

30 **Abstract**

31 Top-down atmospheric inversion infers surface-atmosphere fluxes from spatially

32 distributed observations of atmospheric compositions, which is a vital means for

33 quantifying large-scale anthropogenic and natural emissions. In this study, we

34 developed a Regional multi-Air Pollutant Assimilation System (RAPAS v1.0) based on

35 the Weather Research and Forecasting/Community Multiscale Air Quality Modeling

36 System (WRF/CMAQ) model, the three-dimensional variational (3DVAR) algorithm

37 and the ensemble square root filter (EnSRF) algorithm. It is capable to simultaneously

38 assimilate spatially distributed hourly in-situ measurements of CO, SO_2, NO_2, $PM_{2.5}$

39 and PM_{10} concentrations to quantitatively optimize gridded emissions of CO, SO_2, NO_x,

40 primary $PM_{2.5}$ ($PPM_{2.5}$) and coarse PM_{10} (PMC) on regional scale. RAPAS includes two

41 subsystems, initial field assimilation (IA) subsystem and emission inversion (EI)

42 subsystem, which are used to generate a "perfect" chemical initial condition (IC), and

43 conduct inversions of anthropogenic emissions, respectively. A "two-step" inversion

44 scheme is adopted in the EI subsystem in its each data assimilation (DA) window, in

45 which the emission is inferred in the first step, and then, it is input into the CMAQ

46 model to simulate the initial field of the next window, meanwhile, it is also transferred

47 to the next window as the prior emission. The chemical IC is optimized through the IA

48 subsystem, and the original emission inventory is only used in the first DA window.

49 Besides, a "super-observation" approach is implemented based on optimal estimation

50 theory to decrease the computational costs and observation error correlations and

51 reduce the influence of representativeness errors.

52 With this system, we estimated the emissions of CO, SO_2, NO_x, $PPM_{2.5}$ and PMC in

53 December 2016 over China using the corresponding nationwide surface observations.

54 The 2016 Multi-resolution Emission Inventory for China (MEIC 2016) was used as the

55 prior emission. The system was run from 26 November to 31 December, in which the

56 IA subsystem was run in the first 5 days, and the EI subsystem was run in the following

57 days. The optimized ICs at the first 5 days and the posterior emissions in December

58 were evaluated against the assimilated and independent observations. Results showed

Geoscientific
Model Development
Discussions

Open Access

59   that the root mean squared error (RMSE) decreased by 50.0-73.2%, and the correlation

60   coefficient (CORR) increased to 0.78-0.92 for the five species compared to the

61   simulations without 3DVAR. Additionally, the RMSE decreased by 40.1-56.3%, and

62   the CORR increased to 0.69-0.87 compared to the simulations without optimized

63   emissions. For the whole mainland China, the uncertainties were reduced by 44.4%,

64   45.0%, 34.3%, 51.8% and 56.1% for CO, SO_2, NO_x, $PPM_{2.5}$ and PMC, respectively.

65   Overall, compared to the prior emission (MEIC 2016), the posterior emissions

66   increased by 129%, 20%, 5%, and 95% for CO, SO_2, NO_x and $PPM_{2.5}$, respectively,

67   indicating that there was significant underestimation in the MEIC inventory. The

68   posterior PMC emissions, including anthropogenic and natural dust contributions,

69   increased by 1045%. A series of sensitivity tests were conducted with different

70   inversion processes, prior emissions, prior uncertainties, and observation errors. Results

71   showed that the "two-step" scheme clearly outperformed the simultaneous assimilation

72   of ICs and emissions ("one-step" scheme), and the system is rather robust in estimating

73   the emissions using the nationwide surface observations over China. Our study offers a

74   useful tool for accurately quantifying multi-species anthropogenic emissions at large

75   scales and near-real time.

76

77

78

79

80

81

82

83

84

Geoscientific
Model Development
Discussions

1. Introduction

Due to rapid economic developments and pollution control legislations, an increasing demand to provide updated emission estimates has arisen, especially in areas where anthropogenic emissions are intensive. Accurately estimating source emission quantities and spatiotemporal changes resulting from various regulations is imperative and valuable for understanding air quality responses and crucial for providing timely instructions for the design of future emissions regulations. However, most inventories have been developed based on a bottom-up approach and are usually updated with a few years delay due to the complexity of gathering all statistical information on activity levels and sector-specific emission factors (Ding et al., 2015). The large uncertainty associated with the low temporal and spatial resolution of these datasets also greatly limits the assessment of emission changes. Some studies (Bauwens et al., 2020; Shi and Brasseur, 2020) have evaluated emission changes indirectly through concentration measurements, but air pollution changes are not only dominated by emission changes, but also highly affected by meteorological conditions (Shen et al., 2021).

Top-down atmospheric inversion infers surface-atmosphere fluxes from spatially distributed observations of atmospheric compositions. Recent efforts have focused on developing air pollution data assimilation (DA) system to conduct the top-down inversion, which is able to integrate model and multi-source and large amount observational information to constrain emission sources. Two major methods, namely, 4D-variational data assimilation (4DVAR) and ensemble Kalman filter (EnKF), are widely used in those DA systems. For example, Jiang et al. (2017) used 4DVAR algorithm to estimate global CO emission trends from 2000–2015 using MOPITT retrievals. Kurokawa et al. (2009) and Stavrakou et al. (2008) also used 4DVAR technique to estimate NO_x emission changes. However, the drawback of the 4DVAR method is the additional development of adjoint models that are technically difficult and cumbersome for complex chemical transport models. Instead, EnKF uses the flow-dependent background error covariance generated by ensemble simulations to map the deviations in concentrations to increments of emissions, which is more flexible and

114 easier to implement. Many previous studies have used EnKF techniques to assimilate

115 the single or dual species observations to optmize the corresponding emission species

116 (Chen et al., 2019; Peng et al., 2017; Schwartz et al., 2014; Sekiyama et al., 2010).

117 Multispecies data assimilation has shown the advantage of efficiently reducing the

118 uncertainty in emission inventories and has led to improvements in air quality

119 forecasting (Ma et al., 2019; Miyazaki et al., 2012b), since it would offer additional

120 constraints on emission estimates through the improvements in related atmospheric

121 fields, chemical reactions, and gas-particle transformations (Miyazaki and Eskes, 2013).

122 Barbu et al. (2009) updated sulfur oxide (SO_x) emissions with SO_2 gas and sulfate

123 aerosol observations and showed that forecasts were improved overall but degraded

124 when derived only from SO_2 or sulfate observations.

125 The deviation in chemical initial condition (IC) is one of the important sources of error

126 that affects the accuracy of emission inversion, because atmopheric inversion fully

127 attributes the biases in simulated and observed concentrations to the deviations in

128 emissions (Meirink et al., 2006; Peylin et al., 2005). The biases of concentrations would

129 be compensated through unreasonable adjustment of pollution emissions without the

130 optimization of ICs (Tang et al., 2013). Tang et al. (2011) reported that the simultaneous

131 optimizations of the ICs of O_3, NO_x and volatile organic compounds (VOCs) and the

132 emissions of NO_x and VOCs produced an overall better performance in ozone forecasts

133 than the adjustment in emissions only. Similar method of simultaneously optimizing

134 chemical ICs and emissions were also applied to constraining emissions in many

135 previous studies (Ma et al., 2019; Miyazaki et al., 2012a; Peng et al., 2018). Although

136 a large improvement has been achieved, this method still has great limitations because

137 the contributions from the emissions and the chemical ICs to the model's bias are

138 difficult to distinguish (Jiang et al., 2017). Besides, the simultaneous optimization

139 means that assimilation window is independent with each other, generally, the

140 uncertainties of the emissions cannot be fully corrected in time in a window, resulting

141 in an accumulation of errors in the estimation (Jiang et al., 2021).

142 Since 2013, China has deployed an air pollution monitoring network that publishes

Geoscientific
Model Development
Discussions

143   nationwide and real-time hourly surface atmospheric observations. This dataset

144   provides an opportunity to improve emission estimates using DA. In this study, a

145   regional multi- air pollutant assimilation system introducing 3DVAR and EnKF DA

146   techniques is constructed to simultaneously assimilate various surface observations

147   (e.g., CO, SO_2, NO_2, O_3, $PM_{2.5}$ and PM_{10}). Against the limitations of the simultaneous

148   optimization of emissions and chemical ICs in each DA window (here, named as "one-

149   step" method), a "two-step" approach (Sect. 3) is performed, in which the IC of each

150   DA window is simulated using the posterior emission of the pervious DA window. The

151   capability of RAPAS in reanalysis field generation and emission inversion estimation

152   is evaluated. The robustness of the system is also investigated with different prior

153   inventories, uncertainty settings of the prior emission, and observation errors. This

154   paper is organized as follows: in Sect. 2, we introduce the DA system and the

155   observation data, and in Sect. 3, we describe the experimental design. The results of the

156   system performance and sensitivity runs are presented and discussed in Sect. 4,

157   followed by the conclusions in Sect. 5.

158   **2. Method and data**

159   **2.1 System description**

160   **2.1.1 Procedure of the assimilation system**

161   A regional air pollutant assimilation system has been preliminarily constructed and

162   successfully applied in our previous studies to optimize gridded CO and NO_x emissions

163   (Feng et al., 2020a; Feng et al., 2020b). Herein, the system is further extended to

164   simultaneously assimilate multiple species (e.g., CO, SO_2, NO_2, O_3, $PM_{2.5}$ and PM_{10})

165   and officially named as the Regional multi- Air Pollutant Assimilation System

166   (RAPASv1.0). The RAPAS mainly includes three components: a regional chemical

167   transport model (CTM), which is coupled offline and used to simulate the

168   meteorological fields and atmospheric compositions, and the 3DVAR and ensemble

169   square root filter (EnSRF) modules, which are used to optimize chemical ICs (Feng et

170   al., 2018; Jiang et al., 2013) and anthropogenic emissions (Feng et al., 2020a; Feng et

171   al., 2020b), respectively.

172   Based on above three components, the RAPAS is divided into two subsystems, namely

173   the IC assimilation (IA) subsystem (CTM plus 3DVAR) and the emission inversion (EI)

174   subsystem (CTM plus EnSRF). As shown in Fig. 1, the IA subsystem is run separately

175   to optimize chemical ICs using the CTM model and cycling assimilation within the

176   3DVAR framework (Kleist et al., 2009; Wu et al., 2002). It runs only once and provides

177   a "perfect" chemical ICs for the subsequent EI subsystem. The EI subsystem runs

178   cyclically, and in each cycle (DA window), we use a "two-step" calculation scheme. In

179   the first step, the prior emissions (X^b) are perturbed and put into the CTM model to

180   simulate chemical concentration ensembles, which are then sampled according to the

181   locations and times of the observations. The sampled data together with observations

182   and prior emission ensembles are entered into the EnSRF algorithm to generate the

183   optimized emissions (X^a). In the second step, the optimized emissions are entered again

184   into the CTM model to generate the initial fields of the next DA window. Meanwhile,

185   the optimized emissions are transferred to the next window as the prior emissions,

186   which means that the original emission inventory is only used in the first DA window

187   in the EI subsystem. Different from the synchronously scheme ("one-step" scheme),

188   which only runs the model once and optimizes the ICs of the next window and emission

189   at the same time, this "two-step" scheme needs to run the simulations twice, which is

190   time consuming, but it could transfer the errors in the inverted emissions of current DA

191   window to the next one for further correction. The benefit of this scheme will be further

192   presented in Sect. 4.3.
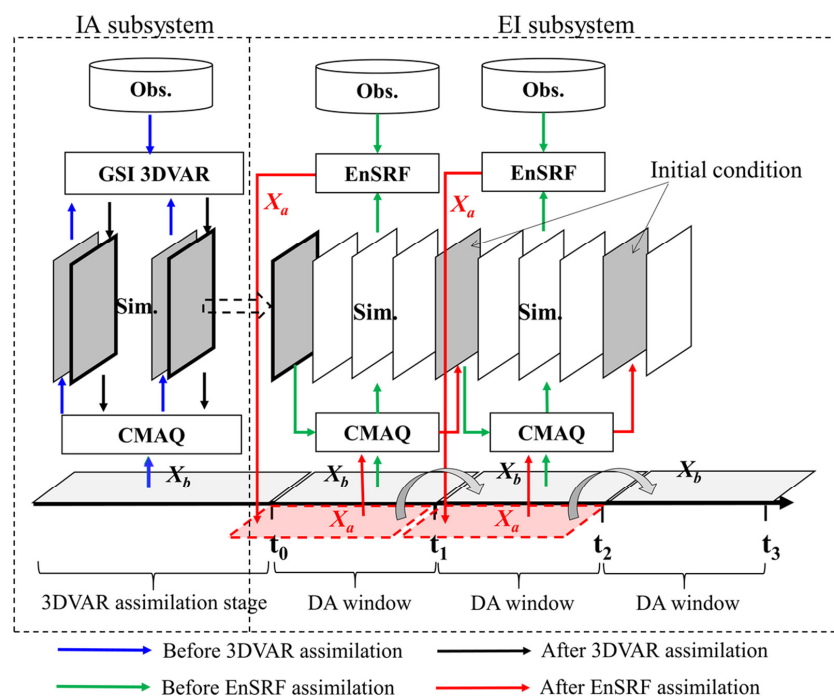
Figure 1. The composition and flow chart of RAPAS.

2.1.2 Atmospheric transport model

The regional chemical transport model of WRF/CMAQ is adopted in this study. CMAQ is a regional 3-D Eulerian atmospheric chemistry and transport model with a "one-atmosphere" design developed in the US Environmental Protection Agency (EPA). It could address the complex interactions among multiple pollutants/air quality issues simultaneously. CMAQ is driven by the WRF model, which is a state of the art mesoscale numerical weather prediction system designed for both atmospheric research and meteorological field forecasting. In this study, WRF version 4.0 and CMAQ version 5.0.2 are adopted. The WRF simulations are performed with a 36-km horizontal resolution on 169×129 grids, and it covers the whole mainland of China (Fig. 2). In the vertical direction, there are 51 sigma levels on sigma-pressure coordinates extending from the surface to 100 hPa. The underlying surface of urban and built-up land is replaced by the MODIS land cover retrieval of 2016 to adapt to the rapid

208 expansion of urbanization. The CMAQ model is run with the same domain but with

209 three grid cells removed from each side of the WRF domain. There are 15 layers in the

210 CMAQ vertical coordinate, which are compressed from the 51 WRF layers.

211 The meteorological initial and lateral boundary conditions are both provided by the

212 Final (FNL) Operational Global Analysis data of the National Center for Environmental

213 Prediction (NCEP) with a $1° × 1°$ resolution at 6-h intervals. The chemical lateral

214 boundary conditions and chemical ICs in the IA subsystem come from the background

215 profiles. As mentioned above, in the EI subsystem, the chemical IC in the first window

216 is provided by the IA subsystem, and in the following windows, it is forward simulated

217 using optimized emission of previous window. The Carbon Bond 05 with updated

218 toluene chemistry (CB05tucl) and the 6th generation aerosol module (AERO6) are

219 chosen as the gas-phase and aerosol chemical mechanisms, respectively (Appel et al.,

220 2013; Sarwar et al., 2012). Detailed physical and chemical configurations are listed in

221 Table 1.

222
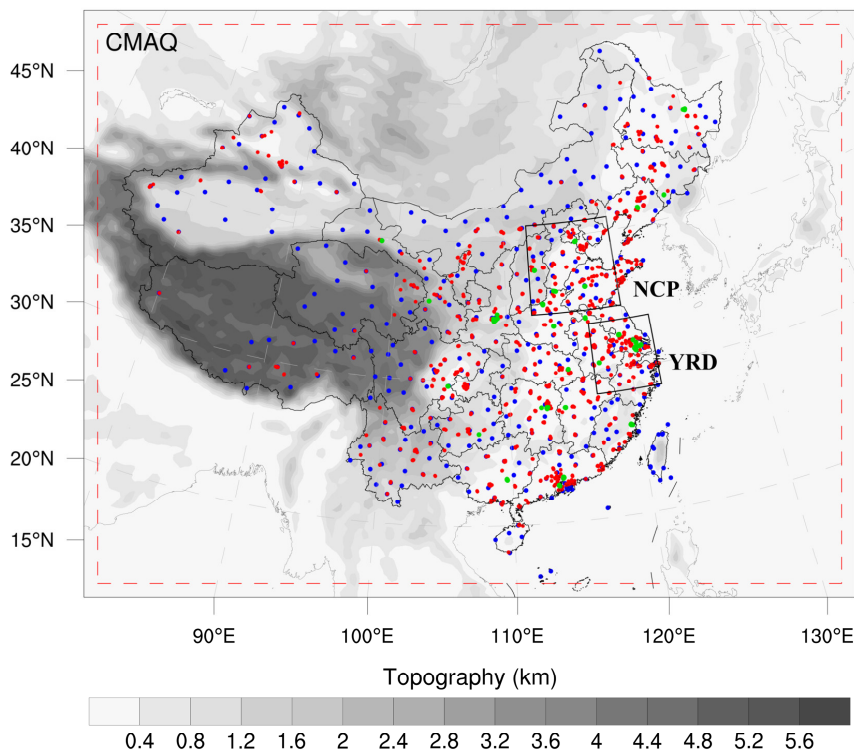
Figure 2. Model domain and observation network. The red dashed frame depicts the CMAQ computational domain; the blue dots represent the meteorological measurement sites; and the red and green dots represent the measurement sites. Observations of all sites are assimilated in the 3DVAR subsystem, while observations of city sites where red dots are averaged are used for assimilation and where green dots are averaged are used for independent evaluation in EI subsystem; the boxed subregions are the North China Plain (NCP) and Yangtze River Delta (YRD); and the shaded area depicts the topography.

231

232

233

234

Geoscientific
Model Development
Discussions

235   **Table 1**. Configuration options of WRF/CMAQ

WRF		CMAQ	
Parameter	Scheme	Parameter	Scheme
Microphysics	WSM6	Horizontal/Vertical advection	yamo/wrf
Longwave	RRTM	Horizontal/Vertical diffusion	multiscale/acm2
Shortwave	Goddard	Deposition	m3dry
Boundary layer	ACM	Chemistry solver	EBI
Cumulus	Kain-Fritsch	Photolysis	phot_inline
Land-surface	Noah	Aerosol module	AERO6
Surface layer	Revised	Cloud module	cloud_acm_ae6
Urban canopy	No	Gas-phase chemistry	CB05tucl

236   **2.1.3 3DVAR assimilation algorithm**

237   The Grid-point Statistical Interpolation (GSI) developed in the US National Centers for

238   Environmental Prediction (NCEP) is employed in this study. Building upon the work

239   of Liu et al. (2011), Jiang et al. (2013) and Feng et al. (2018), we extended it to

240   simultaneously assimilate multiple species (including CO, SO_2, NO_2, O_3, $PM_{2.5}$, and

241   PM_{10}) and first used individual aerosol species of $PM_{2.5}$ as analysis variables within the

242   GSI/WRF/CMAQ framework. Additional works include the construction of surface air

243   pollutant observation operators, the updating of observation errors, and the statistics of

244   background error covariance for the analysis variables. Moreover, the data interface is

245   also modified to read/write the CMAQ output/input file directly, which is easy to

246   implement.

247   In the sense of a minimum analysis error variance, the 3DVAR algorithm optimizes

248   analysis fields with observations by iterative processes to minimize the cost function

249   (J(x)) defined below:

250    $$J(x) = \frac{1}{2}(\mathbf{x_a} - \mathbf{x_b})^T \mathbf{B}^{-1}(\mathbf{x_a} - \mathbf{x_b}) + \frac{1}{2}[H(\mathbf{x_a}) - \mathbf{y}]^T \mathbf{R}^{-1}[H(\mathbf{x_a}) - \mathbf{y}], \qquad (1)$$

251   where $\mathbf{x_a}$ is a vector of the analysis field; $\mathbf{x_b}$ denotes the background field; $\mathbf{y}$ is the

252   vector of observations; $\mathbf{B}$ and $\mathbf{R}$ are the background and observation error covariance

253   matrices, respectively, representing the relative contributions to analysis; and H is the

254   observation operator that maps the model variables to the observation space.

255   The analysis variables are the 3D mass concentrations of the pollution compositions

256   (e.g., CO and sulfate) at each grid point. Hourly surface pollution observations within

257   1 hour window of the analysis are assimilated. To assimilate the surface pollution

258   observations, model-simulated compositions are first diagnosed at the observation

259   locations. For gas pollutions that are directly used as analysis variables, data units need

260   to be converted from ppm or ppb to mg m^{-3} or μg m^{-3} to match with observations. The

261   model-simulated PM$_{2.5}$ and PM$_{10}$ concentrations at the ground level are diagnosed as

262   follows:

263    $PM_{2.5} = f_i \times PM_i + f_j \times PM_j + f_k \times PM_k = OC + EC + SO_4^{2-} + NO_3^- + NH_4^+ +$

264    $SEAS + AP_{2.5}$ (2)

265    $PM_{10} = PM_i + PM_j + PM_k = PM_{2.5} + PMC$ (3)

266   where f_i, f_j, and f_k are the PM$_{2.5}$ fractions of the Aitken, accumulation, and coarse

267   modes, respectively. These ratios are recommended as the concentrations of PM$_{2.5}$ and

268   fine mode aerosols (i.e., Aitken plus accumulation) could differ because the PM$_{2.5}$

269   particles include small tails from the coarse mode in the CMAQ model (Binkowski and

270   Roselle, 2003; Jiang et al., 2006). PM_i, PM_j, and PM_k represent the mass

271   concentrations of the 3 modes in the CMAQ model. Seven aerosol species of PM$_{2.5}$,

272   including organic carbon (OC), elemental carbon (EC), sulfate (SO_4^{2-}), nitrate (NO_3^-),

273   ammonium (NH_4^+), sea salt (SEAS), and fine-mode unspeciated aerosols ($AP_{2.5}$), and

274   additional coarse PM$_{10}$ (PMC) are extracted as analysis variables, which are updated

275   by the PM$_{2.5}$ and PMC observations, respectively. Before the calculation of equation (1)

276   within the GSI, the analysis variables are bilinearly interpolated in the horizontal

277   direction to the observation locations.

278   The computation of background error covariance (**B**) is generally costly and difficult

279   when a high-dimensional numerical model is used. For simplification, **B** is represented

280   as a product of spatial correlation matrices and standard deviations (SDs):

281    $$\mathbf{B} = \mathbf{D}\mathbf{C}\boldsymbol{D}^T \tag{4}$$

282    $$\mathbf{C} = \boldsymbol{C_x} \otimes \boldsymbol{C_y} \otimes \boldsymbol{C_z} \tag{5}$$

283   where **D** is the background error SD matrix, **C** is the background error correlation

284   matrix, $\otimes$ denotes the Kronecker product, and $\boldsymbol{C_x}$, $\boldsymbol{C_y}$, and $\boldsymbol{C_z}$ denote three one-

285   dimensional correlation submatrices in the longitude, latitude, and vertical coordinate

286   directions, respectively. $\boldsymbol{C_x}$ and $\boldsymbol{C_y}$ are assumed to be isotropic horizontally such that

287   can be represented using a Gaussian function. The correlation between any two points

288   x_i and x_j in the horizontal can be expressed as follows:

289    $$c(x_i,\ x_j) = e^{-\frac{(x_i - x_j)^2}{2L^2}} \tag{6}$$

290   where L is the horizontal correlation scale, which is estimated using the proxy of the

291   background error (Fig. 3). The vertical correlation matric $\boldsymbol{C_z}$ is directly estimated from

292   the model background field since $\boldsymbol{C_z}$ is only an $n_z \times n_z$ (here, n_z=15) matrix.
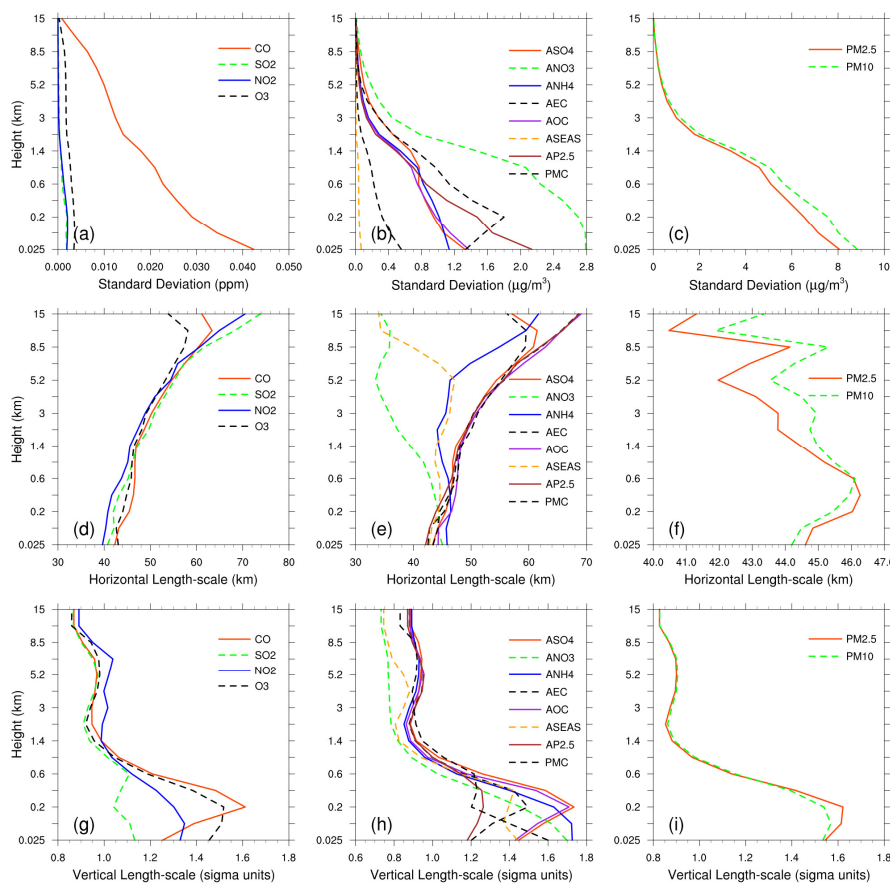
Figure 3. Vertical profiles of standard deviations (top, μg m^{-3}), horizontal length scale (middle, km) and vertical length scale (bottom, km) for CO, SO$_2$, NO$_2$, O$_3$, sulfate, nitrate, ammonium, EC, OC, sea salt, unspeciated aerosols (AP2.5), PMC, PM$_{2.5}$ and PM$_{10}$.

To estimate these matrices, the "NMC" method is used here to compute **B** for each variable by taking the differences between forecasts of different lengths valid at the same time (Parrish and Derber, 1992; Rabier et al., 1998). Differences between 24- and 12-h WRF/CMAQ forecasts of 60 pairs (two pairs a day) of analysis variables valid at either 0000 or 1200 UTC over November 2016 are used. The horizontal and vertical length scales of the correlation matrices are estimated by recursive filters (Purser et al., 2003). The vertical distribution of background error SDs is shown in Fig. 3, which

305   varies with height and species. The vertical profile of the background error SDs

306   corresponds to the vertical concentration distribution. This means that higher

307   concentrations tend to have larger background error SDs (e.g., CO and nitrate). These

308   SDs exhibit a common reduction with height, especially at the top of the boundary layer.

309   The horizontal correlation of background error determines the propagation of

310   observation information in this direction, while vertical correlation determines the

311   vertical extension of such increments. For gaseous pollutants and individual aerosol

312   components, excluding nitrate and sea salt, the horizontal length scales decrease with

313   increasing heights, while the total particulate matter increases slightly under the

314   boundary layer and then decreases slightly over the boundary layer. The ground-level

315   scale generally spread 40-45 km for all control variables on average. The vertical length

316   scale of most species increases with height near the ground where they are emitted

317   (Descombes et al., 2015) and then drops rapidly to the height of the upper stable

318   atmosphere, with a scale of 1.4 km.

2.1.4 EnKF assimilation algorithm

320   In EnKF, the time-dependent uncertainties of the state variables are estimated using a

321   Monte Carlo approach through an ensemble. Uncertainty can be propagated with linear

322   or nonlinear dynamic models (flow-dependent background error covariance) by simply

323   implementing ensemble simulations. The EnSRF algorithm introduced by (Whitaker

324   and Hamill, 2002) is used to constrain pollution emissions in this study. EnSRF is a

325   deterministic EnKF that obviates the need to perturb observations, which has a higher

326   computational efficiency and a better performance (Sun et al., 2009).

327   The perturbation of prior emissions represents the uncertainty. We implement additive

328   emission adjustment methods, which are calculated using the following function.

$$X_i^b = X_0^b + \delta X_i^b, \text{i} = 1, 2, ..., \text{N} \tag{7}$$

330   where b represents the background (prior) state, i is the identifier of the perturbed

331   samples, N is the ensemble size (40 in this study), and δX_i^b represents the randomly

332   perturbed samples that are added to the prior emissions X_0^b to produce ensemble

333   samples of the inputs X_i^b. δX_i^b is drawn from Gaussian distributions with a mean of

334   zero and the standard deviation of the prior emission uncertainty in each grid. The state

335   variables of the emissions include CO, SO_2, NO_x, primary $PM_{2.5}$ ($PPM_{2.5}$) and PMC.

336   We used variable localization to update the analysis, which means that the covariance

337   among different state variables is set to zero (Miyazaki et al., 2012b).

338   After obtaining an ensemble of state vectors (prior emissions), ensemble runs of the

339   CMAQ model are conducted to propagate these errors in the model with each ensemble

340   sample of state vectors. Combined with observational vector y, the state vector is

341   updated by minimizing the analysis variance:

342
$$\overline{X^a} = \overline{X^b} + K(y - H\overline{X^b}) \tag{8}$$

343
$$K = P^b H^T (H P^b H^T + R)^{-1} \tag{9}$$

344
$$P^b = \frac{1}{N-1} \sum_{i=1}^{N} (X_i^b - \overline{X^b})(X_i^b - \overline{X^b})^T \tag{10}$$

345
$$\delta X_i^a = \delta X_i^b - \widetilde{K} H \delta X_i^b \tag{11}$$

346   While employing sequential assimilation and independent observations, $\widetilde{K}$ is

347   calculated as follows:

348
$$\widetilde{K} = \left(1 + \sqrt{R / {H P^b H^T + R}}\right)^{-1} K \tag{12}$$

349   where $\overline{X^b}$ represents the mean of the ensemble samples; P^b is the ensemble-

350   estimated background (a priori) error covariance; $P^b H^T$ contains the response of the

351   uncertainty in the simulated concentrations to the uncertainty in emissions; K is the

352   Kalman gain matrix of the ensemble mean depending on the P^b and observation error

353   covariance R, representing the relative contributions to analysis; and $\widetilde{K}$ is the Kalman

354   gain matrix of the ensemble perturbation, which is used to calculate emission

355   perturbations after inversions δX_i^a. The ensemble mean $\overline{X^a}$ of the analyzed state is

356   taken as the best estimate of the emissions.

357 With large volumes of site observations that are recorded at a much higher resolution

358 than the model grid spacing, there would be significant correlated or fully consistent

359 model-data mismatch errors in one cluster, resulting in excessive adjustments and

360 deteriorated model performances (Houtekamer and Mitchell, 2001). To reduce the

361 horizontal observation error correlations and the influence of representativeness errors,

362 a "super-observation" approach combining multiple noisy observations located within

363 the same grid and assimilation window is developed based on optimal estimation theory

364 (Miyazaki et al., 2012a). Previous studies have demonstrated the necessity of data-

365 thinning and dealiasing errors (Feng et al., 2020b; Zhang et al., 2009a). The super-

366 observation y_{new}, super-observation error r_{new} and corresponding simulation $x_{new,i}$

367 of the ith sample are calculated as follows:

368
$$1/r_{new}^2 = \sum_{j=1}^m 1/r_j^2 \tag{13}$$

369
$$y_{new} = \sum_{j=1}^m w_j\, y_j / \sum_{j=1}^m w_j \tag{14}$$

370
$$x_{new,i} = \sum_{j=1}^m w_j\, x_{ij} / \sum_{j=1}^m w_j \tag{15}$$

371 where j is the identifier of m observations within a super-observation grid; r_j is the

372 observational error of actual jth observation y_j; x_{ij} represents a simulated

373 concentration using the ith prior emission sample corresponding to the jth observation;

374 and $w_j = 1/r_j^2$ is the weighting factor. The super-observation error decreases as the

375 number of observations used within a super-observation increases. This method has

376 been used in our previous inversions using surface-based (Feng et al., 2020b) and

377 satellite-based (Jiang et al., 2021) observations.

378 In this study, the DA window is set to 1 day because the model needs a longer time to

379 integrate emission information into the concentration ensembles (Ma et al., 2019). In

380 addition, due to the complexity of hourly emissions, it is very difficult to simulate

381 hourly concentrations that can match the observations well. Although a longer DA

382 window could allow more observations to constrain the emission change of one grid,

383 the spurious correlation signals of EnKF would attenuate observation information with

384 time (Bruhwiler et al., 2005; Jiang et al., 2021). Kang et al. (2012) and Zhang et al.

385 (2015) also pointed out that the emission inversion with a long window (e.g., 1 to 3

386 weeks) is not as accurate as that obtained with a short DA window (e.g., 6 hours to 1

387 week). Therefore, daily mean simulations and observations are used in the EnSRF

388 algorithm, and daily emissions are optimized in this system.

389 EnKF is subject to spurious correlations due to the limited number of ensembles when

390 it is applied in high-dimensional atmospheric models, which can cause rank

391 deficiencies in the estimated background error covariance and filter divergence, and

392 further degrade analyses and forecasts (Wang et al., 2020). Covariance localization is

393 performed to reduce spurious correlations caused by the finite ensemble size

394 (Houtekamer and Mitchell, 2001). Covariance localization preserves the meaningful

395 impact of observations on state variables within a certain distance (cutoff radius) but

396 limits the detrimental impact of observations on remote state variables. The localization

397 function of Gaspari and Cohn function (Gaspari and Cohn, 1999) is used in this system,

398 which is a piecewise continuous fifth-order polynomial approximation of a normal

399 distribution. The optimal localization scale is related to the ensemble size, assimilation

400 window, dynamic system, and lifetime of a chemical species in the atmosphere. CO,

401 SO_2 and $PM_{2.5}$ are rather stable in atmosphere, with lifetime more than 1 day. According

402 to the averaged wind speed (3.3 m/s, Table 4) and the length of DA window, their

403 localization scales are set to 300 km. In addition, NO_2 is rather active, with a lifetime

404 of approximately 10 hours in winter (de Foy et al., 2015), and PMC, which is mainly

405 from local sources, its residence time in the atmosphere is also short due to the rapid

406 deposition rate (Clements et al., 2014; Clements et al., 2016; Hinds, 1982). Their

407 localization scales are set to 150 km and 250 km, respectively.

408 **2.2 Prior emissions and uncertainties**

409 The anthropogenic emissions over China are taken from the 2016 Multi-resolution

410 Emission Inventory for China (MEIC 2016) (Zheng et al., 2018), while those over the

411   other regions of East Asia are obtained from the mosaic Asian anthropogenic emission

412   inventory (MIX) (Li et al., 2017). The spatial resolutions of both the MEIC and MIX

413   inventories are 0.25° × 0.25°, and they are both downscaled to match the model grid

414   spacing (36 km). The spatial distributions of the CO, SO_2, NO_x, $PPM_{2.5}$ and PMC

415   emissions are shown in Fig. 10. The daily emission inventory, which is arithmetic

416   averaged from the combined monthly emission inventory, is directly used in the EI

417   subsystem and employed as the prior emission of the first DA window in the EI

418   subsystem (Fig. 1). MEIC 2012 is used as an alternative a priori over China to

419   investigate the impact of different prior emissions on the optimized emissions. The

420   Model of Emissions of Gases and Aerosols from Nature (MEGAN) (Guenther et al.,

421   2012) is used to calculate time-dependent biogenic emissions. It is also driven by the

422   WRF model in this study. Biomass burning emissions are not included because they

423   have little impact across China during the study period (Zhang et al., 2020).

424   During the cycling inversions, the inverted emissions of different members converge

425   gradually, and the ensemble-estimated error covariance matrix is very likely to be

426   underestimated. To avoid this, considering the compensation of model errors and

427   comparable emission uncertainties from one day to the next, we impose the same

428   uncertainty on emissions at each DA window. As mentioned above, the optimized

429   emissions of the current DA window are transferred to the next DA window as prior

430   emissions. The technology-based emission inventory developed by Zhang et al. (2009b),

431   basically using the same method as MEIC, shows that the emissions of PMC and $PPM_{2.5}$

432   have the largest uncertainties, followed by CO, and finally SO_2 and NO_x. Therefore, the

433   uncertainties in this study are set to 40%, 40%, 30%, 25%, and 25%. However, previous

434   studies have shown that the inversely estimated CO and PMC emissions could exceed

435   100% higher than the bottom-up emissions (MEIC) in certain areas (Feng et al., 2020b;

436   Ma et al., 2019). According to the extent of underestimation, we set an uncertainty of

437   100% for both the CO and PMC emissions at the beginning of the three DA windows

438   to quickly converge the emissions. The mean emission analysis is generally minimally

439   sensitive to the uncertainty setting in our cycle assimilation method (Feng et al., 2020;

Geoscientific
Model Development
Discussions

440   Gurney et al., 2004; Miyazaki et al., 2012) because the inversion errors of the current

441   window could be transferred to the next window for further optimization (Sect. 4.3).

2.3 Observation data and errors

443   Hourly averaged surface CO, SO_2, NO_2, O_3, $PM_{2.5}$ and PM_{10} observations from 1504

444   national control air quality stations are assimilated in this system, which were obtained

445   from the Ministry of Ecology and Environment of the People's Republic of China

446   (http://106.37.208.233:20035/). These sites distribute over most of central and eastern

447   China and become denser near metropolitan areas (see Fig. 2). Value-range and time-

448   continuity checks are performed to ensure data quality. Value-range checks are mainly

449   performed to eliminate unrealistic or nonspatially representative observations. Only

450   observations within the subjectively selected threshold range are assimilated (Table 2).

451   A time-continuity check is performed to eliminate gross outliers and a sudden anomaly

452   using a function of $|O(t) - O(t \pm 1)| \leq f(t)$, where $O(t)$ and $O(t \pm 1)$ represent

453   observations at time t and t+1, respectively, and $f(t) = T_a + T_b \times O_t$. T_b is fixed to

454   0.15, and the section of T_a is given in Table 2, which is determined empirically

455   according to the time series change of concentration at each site. It should be noted that,

456   to avoid potential cross-correlations, we assimilated $PM_{2.5}$ and PMC. Additionally, in

457   the EI subsystem, the observations within each city are averaged to thin the data density

458   and reduce the error correlation (Houtekamer and Mitchell, 2001; Houtekamer and

459   Zhang, 2016). Finally, 336 city sites are available across the mainland of China, in

460   which 311 cities' data are selected for assimilation and the remaining 25 are selected

461   for independent validation (Fig. 2). In the IA subsystem, due to the small horizontal

462   correlation scale (Fig. 3), to obtain more extensive observation constraints, all site

463   observations are assimilated to provide a "perfect" IC for the next emission inversion.

464   The observation error covariance matrix (**R**) includes both measurement and

465   representation errors. The measurement error ε_0 is defined as follow:

$$\varepsilon_0 = ermax + ermin \times \Pi_0 \qquad (16)$$

467   where $ermax$ is a base error, and Π_0 denotes the observed concentration. These

468   parameters for different species are listed in Table 2, which are determined according

469   to Chen et al. (2019), Feng et al., (2018) and Jiang et al. (2013).

470   The representative error depends on the model resolution and the characteristics of the

471   observation locations, which is calculated using the equations of Elbern et al. (2007)

472   defined as follows:

473
$$\varepsilon_r = \gamma \varepsilon_0 \sqrt{\Delta l / L} \qquad (17)$$

474   where γ is a tunable parameter (here, γ=0.5), Δl is the grid spacing (36 km), and L

475   indicates the radius (here, 3 km for simplification) of influence area of an observation.

476   The total observation error (r) is defined as follows:

477
$$r = \sqrt{\varepsilon_0^2 + \varepsilon_r^2} \qquad (18)$$

478   **Table 2**. Parameters of quality control and measurement error

Parameter	CO mg m^{-3}	SO$_2$ µg m^{-3}	NO$_2$ µg m^{-3}	O$_3$ µg m^{-3}	PM$_{2.5}$ µg m^{-3}	PMC µg m^{-3}
value-range	0.1-12	1-800	1-250	1-250	1-800	1-900
time-continuity (T_a)	2.5	160	70	80	180	180
ermax	0.05	1	1	1	1.5	1.5
ermin	0.5%	0.5%	0.5%	0.5%	0.75%	0.75%

479   **3 Experimental design**

480   RAPAS is conducted according to the procedure and settings described in Sect. 2. The

481   IA subsystem is run from 26 to 31 November 2016 with a 6-hour interval cycling

482   assimilation to optimize ICs (ICDA). A better IC at 0000 UTC on December 1 can be

483   obtained by 5-day high-frequency cycling assimilation and atmospheric mixing. Then

484   the EI subsystem is run for December 2016 with a 1-day assimilation window to

485   optimize emissions (EMDA). Both assimilation experiments use the combined prior

486   emission inventories of 2016 as described in Sect. 2.2, and the emission base year

487   coincides with the research stage. To evaluate the IC improvements from the IA

488   subsystem, an experiment without 3DVAR (ICNO) is conducted with the same

489   meteorological fields and physical and chemistry parameterization settings as those of

490   the ICDA. To evaluate the posterior emissions of the EI subsystem, two parallel forward

491   modeling experiments are performed for December 2016, namely, a control experiment

492   (CEP) with prior (MEIC 2016) emissions and a validation experiment (VEP) with

493   posterior emissions. Both experiments use the same initial field at 0000 UTC on

494   December 01 generated through the IA subsystem. Similar to the above, the only

495   differences between CEP and VEP are emissions. Table 3 gives a summary of these

496   different simulation experiments.

497   To investigate the robustness of our system, 7 sensitivity tests (from EMS1 to EMS7,

498   see Table 3) are performed. These experiments are all based on EMDA. In EMS1, rather

499   than forward simulated using the optimized emissions of the previous DA window in

500   EMDA, the initial fields of each DA window are optimized using the 3DVAR algorithm

501   directly and the observations at the corresponding moment as mentioned in Sect. 2.3.

502   The objective of this experiment is to investigate the advantages of the "two-step"

503   calculation scheme in the EI subsystem as introduced in Sect. 2.1. EMS2 uses MEIC

504   2012 as the original prior emission in China, aiming to investigate the impact of

505   different prior inventories on the estimates of emissions. Four other experiments,

506   namely EMS3-6, aim to test the impact of different prior uncertainty settings, in which,

507   the prior uncertainties are reduced by -50% and -25%, and increased by 25% and 50%,

508   respectively. EMS7 aims to evaluate the impact of observation errors on emission

509   estimates, in which all the observation errors are magnified twice. Seven forward

510   modeling experiments (VEP1, VEP2, …, VEP7) are also performed with posterior

511   emissions of EMS1 to EMS7 to evaluate their performances, respectively.

512

513

514

515

516   **Table 3**. Experiments conducted in this study

Exp. Type	Exp. Name	Period	Initial field	Emission	IA	EI
Assimilation	ICDA	26-31 November	previous 6-hr interval cycling forecast	MEIC 2016 for November	YES	NO
	EMDA	1-31 December	0000 UTC on December 1, taken from ICDA	MEIC 2016 for December (the first DA window), optimized emissions of the previous window (other DA windows)	NO	YES
Sensitivity	EMS1	1-31 December	Forecast with prior emissions in the previous window	The same as EMDA	YES	YES
	EMS2	1-31 December	The same as EMDA	The same as EMDA, but for EMIC 2012	NO	YES
	EMS3-6	1-31 December	The same as EMDA	The same as EMDA, but with a $\pm$ 25% or $\pm$ 50% of default uncertainty	NO	YES
	EMS7	1-31 December	The same as EMDA	The same as EMDA, but with a +100% of default observation errors	NO	YES
Verification	ICNO	26-31 November	The same as ICDA	The same as ICDA	NO	NO
	CEP	1-31 December	The same as EMDA	MEIC 2016 for December	NO	NO
	VEP	1-31 December	The same as EMDA	Posterior emissions of EMDA	NO	NO
	VEP1-7	1-31 December	The same as EMDA	Posterior emissions of EMS1-7	NO	NO

517   # 4 Results

518   ## 4.1 Evaluations

519   ### 4.1.1 Simulated meteorological fields

520   In the RAPAS system, the inversion approach attributes all the biases between the

521   simulated and observed concentrations to the emissions. The meteorological fields

522   dominate the physical and chemical processes of the air pollutants in the atmosphere,

523   and thus their simulation accuracy would significantly affect the estimates of emissions

524   in this study. To quantitatively evaluate the performance of the WRF simulations, the

525   mean bias (BIAS), root mean square error (RMSE), and correlation coefficient (CORR)

526   were calculated against the surface meteorological observations measured at 400

527   stations, which were obtained from the National Climate Data Center (NCDC)

528   integrated surface database (http://www.ncdc.noaa.gov/oa/ncdc.html). The spatial

529   distribution of the meteorological stations (blue dots) is shown in Fig. 2. The simulated

530   temperature at 2 m (T2), relative humidity at 2 m (RH2), and wind speed at 10 m (WS10)

531   from 26 November to 31 December 2016 are evaluated against the observations. Table

532   4 summarizes the statistical results of the evaluations of the simulated meteorological

533   parameters. Overall, the T2 and RH2 are slightly underestimated, with biases of -0.1 °C

534   and -3.8%, respectively. The CORRs are approximately 0.98 for T2 and 0.94 for RH2,

535   showing good consistency between the observations and simulations. The WS10 is

536   overestimated, with a bias of 0.7 m/s and an RMSE of 0.8 m/s, but is better than many

537   other studies (Chen et al., 2016; Jiang et al., 2012a; Jiang et al., 2012b). Therefore,

538   WRF can generally reproduce the meteorological conditions sufficiently in terms of

539   their temporal variation and magnitude over China, which is adequate for our inversion

540   estimation.

541   **Table 4**. Statistics comparing the simulated and observed 10-m wind speed (WS10,

542   m/s), 2-m temperature (T2, °C), and 2-m relative humidity (RH2, %) averaged over all

543   400 stations.

Variable Met.	Mean Obs.	Mean Sim.	BIAS	RMSE	CORR
WS10 (m/s)	2.6	3.3	0.7	0.8	0.72
T2 (°C)	2.9	2.8	-0.1	0.7	0.98
RH2 (%)	66.3	62.6	-3.8	5.2	0.94

544   * BIAS, mean bias; RMSE, root mean square error; CORR, correlation coefficient

4.1.2 Initial fields

Figure 4 shows the evaluations of the analyzed concentrations of the 6 species against surface observations. For comparison, the evaluations of the simulations without 3DVAR (ICNO) are also shown in Fig. 4. The simulations of the ICNO experiment (red dots) are scattered on both sides of a central line, as large systematic biases remain across many measurement sites. Conversely, the ICDA experiment (blue dots) shows much better agreement with observations than those from ICNO. The statistics show that there are large systematic biases in the ICNO simulations, with large RMSEs and small CORRs for all species, especially for CO and PMC. After the assimilation of surface observations, the RMSE of CO decreases to 0.7 mg m^{-3}, and those of SO_2, NO_2, O_3, $PM_{2.5}$ and PMC decrease to 22.0, 12.0, 9.6, 20.5 and 19.6 μg m^{-3}, respectively, with respective reduction rates of 50.0%, 73.1%, 61.0%, 64.7%, 69.5%, and 60.8% compared to the ones of the ICNO (Table 5). The CORRs of ICDA increase by 290.0%, 291.3%, 55.4%, 87.2%, 130.0% and 214.8% to 0.78, 0.90, 0.87, 0.88, 0.92 and 0.85, respectively. These statistics indicate that the initial fields can be adjusted effectively by our IA subsystem.
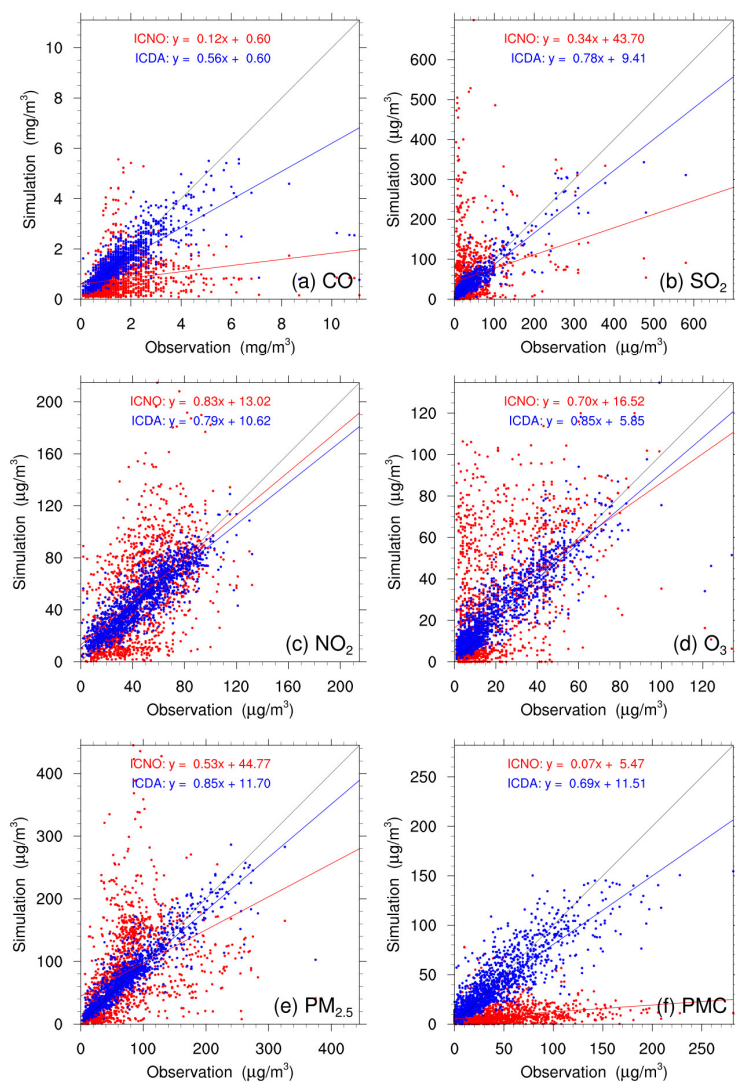
Figure 4. Scatter plots of simulated versus observed (a) CO, (b) SO_2, (C) NO_2, (d) O_3, (e) $PM_{2.5}$ and (f) PMC mass concentrations at 0000 UTC on December 1 initializations from the background (red) and analysis (blue) fields.

Geoscientific
Model Development
Discussions

567 **Table 5**. Comparisons of the surface CO, SO_2, NO_2, O_3, $PM_{2.5}$ and PMC mass

568 concentrations from the control and assimilation experiment against observations

569 aggregated over all analysis times. CO unit: mg m^{-3}; others units: μg m^{-3}.

Species	Exp. Name	Mean Obs.	Mean Sim.	BIAS	RMSE	CORR
CO	ICNO	1.5	0.8	-0.7	1.4	0.20
	ICDA		1.5	-0.1	0.7	0.78
SO_2	ICNO	36.3	56.0	19.7	81.7	0.23
	ICDA		37.8	1.5	22.0	0.90
NO_2	ICNO	45.8	51.1	5.3	30.8	0.56
	ICDA		47.0	1.1	12.0	0.87
O_3	ICNO	20.5	30.8	10.4	27.2	0.47
	ICDA		23.3	2.8	9.6	0.88
$PM_{2.5}$	ICNO	70.9	82.2	11.3	67.3	0.40
	ICDA		71.8	0.9	20.5	0.92
PMC	ICNO	43.5	8.5	-35.0	50.0	0.27
	ICDA		41.6	-1.9	19.6	0.85

570 * BIAS, mean bias; RMSE, root mean square error; CORR, correlation coefficient

571 **4.1.3 Posterior emissions**

572 Due to mismatched spatial scales, it is difficult to directly evaluate the optimized

573 emissions against observations. Generally, we indirectly validate them by comparing

574 the forward simulated concentrations using the posterior emissions against atmospheric

575 measurements (e.g., Jiang et al. (2014), Jin et al. (2018), and Peters et al. (2007)). Figure

576 5 shows the spatial distributions of the mean biases between the simulated gaseous

577 pollutants using prior and posterior emissions and assimilated observations. In the CEPs,

578 for each species, the distribution of biases is similar to the increments in background

579 fields constrained through 3DVAR as shown in Fig. S1. For example, almost all sites

580 have large negative biases for CO, while for SO_2 and NO_2, positive biases are mainly

581 distributed over the North China Plain (NCP), Yangtze River Delta (YRD), Sichuan

582 Basin (SCB) and Central China, and negative biases are over the rest areas. After

583 constraining with observations, the biases of all the 3 gaseous air pollutants are

584   significantly reduced in most sites. For CO, the biases at 62% of the sites decreased to

585   absolute values less than 0.2 mg m^{-3}, and for SO_2 and NO_2, the biases at 52% and 47%

586   of the sites were within ±4 µg m^{-3}. However, large negative biases are still observed in

587   part of western Chinas, indicating that the uncertainties of the posterior emissions are

588   still large in western China, which may be attributed to the large biases in prior

589   emissions and to the relatively limited observation. Overall, the statistics show that

590   there are different levels of improvements at 92%, 85% and 85% of the total 311

591   assimilation sites for CO, SO_2 and NO_2, respectively. The small amount of sites with

592   worse performance may be related to the overadjusted emissions by EI or contradictory

593   adjustments caused by opposite biases in adjacent areas.

594   Table 6 lists the statistical results of the evaluations averaged over the whole mainland

595   of China. For CO, the mean bias is -0.8 mg m^{-3} with the prior emissions, while it

596   substantially reduces to -0.1 mg m^{-3} with a reduction rate of 89.6% when simulating

597   with the posterior emissions. Additionally, the RMSE decreases by 48.1% from 1.08 to

598   0.56 mg m^{-3}, and the CORR increases by 76.1% from 0.46 to 0.81. For SO_2 and NO_2,

599   the regional mean biases slightly increase as the positive/negative biases among

600   different sites might be offset. However, the RMSEs decrease to 17.7 and 12.3 µg m^{-3},

601   respectively, which are 58.3% and 50.8% lower than those of CEPs, and the CORRs

602   increase by 125.6% and 35.4%, both reaching up to 0.88, indicating that EI has

603   significantly improved the NO_x and SO_2 emission estimates.
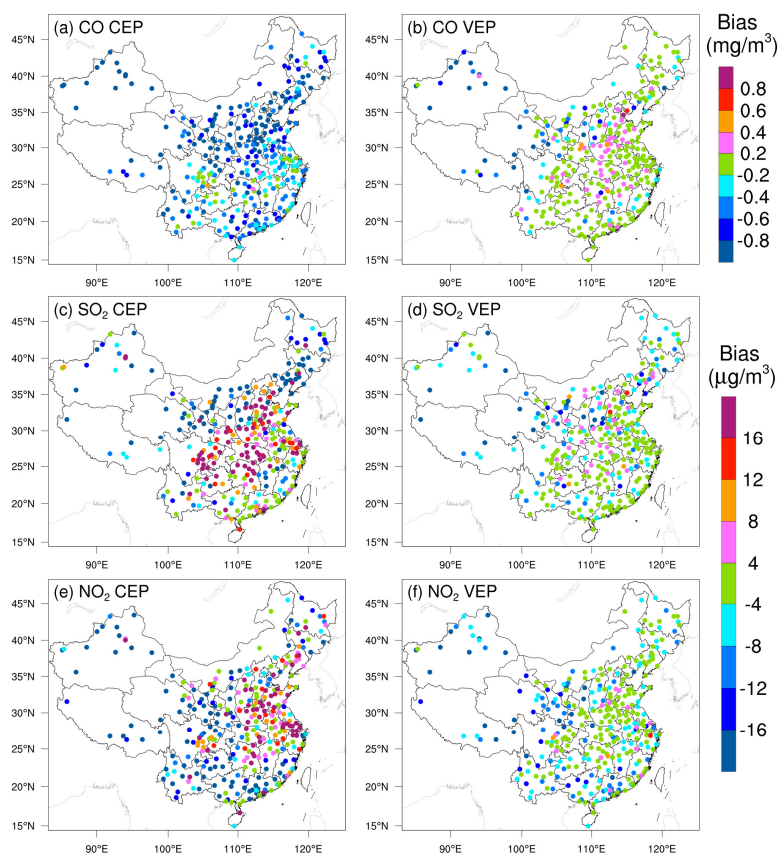
Figure 5. Spatial distribution of the BIAS of the simulated (a, b) CO, (c, d) SO_2 and (e, f) NO_2 with prior (left, CEP) and posterior (right, VEP) emissions. CO unit: mg m^{-3}; SO_2 and NO_2 units: μg m^{-3}.

Figure 6 shows the spatial distributions of the mean biases of simulated $PM_{2.5}$ and PMC evaluated against the assimilated observations. Similarly, the CEP simulations do not perform well. There are widespread underestimations across the country, with mean biases of -24.0 and -32.4 μg m^{-3}. After data assimilation, the performance of VEP simulations is significantly improved. The biases decrease by 72.1% and 90.4% to -6.7 and -3.1 μg m^{-3}, the RMSEs decrease by 41.2% and 40.7% to 29.6 and 24.6 μg m^{-3}, and the CORRs increase by 35.9% and 176.0% to 0.87 and 0.69 for $PM_{2.5}$ and PMC, respectively. Overall, 89.6% and 97.2% of the assimilation sites are improved for $PM_{2.5}$

616 and PMC, respectively. However, compared with the results of the 3 gaseous pollutants,

617 there are sites with large biases scattered throughout the whole domain. Besides the

618 potential overadjusted or contradictory adjustments of emissions as in the 3 gas species,

619 it may be also related to the complex precursors and the nonlinear responses to its

620 precursors for $PM_{2.5}$, and the fact that we do not simulate the time variation of dust

621 blowing caused by wind speed for PMC due to the lack of land cover data that is

622 compatible with the CMAQ dust module and agricultural activities data to identify dust

623 source regions.
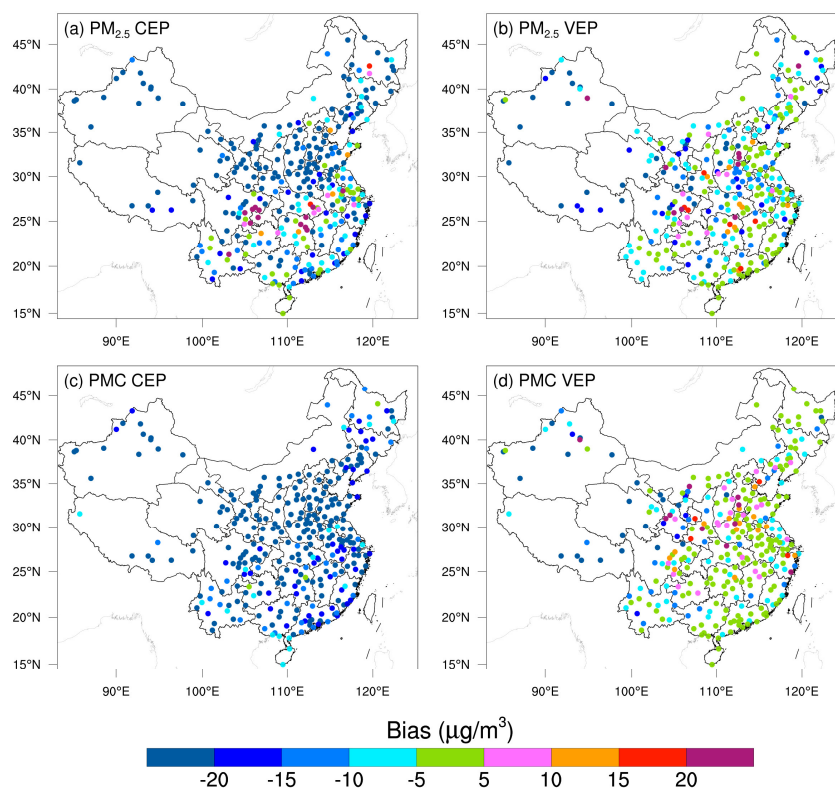
624

625 **Figure 6**. Same as in Fig. 5 but for $PM_{2.5}$ and PMC.

626 Figure 7 and Fig. 8 show the spatial distributions of the biases calculated against the

627 independent observations for the 5 species. With posterior emissions, the decreasing

628   ratios of RMSEs range from 26.7% to 42.0%, and the CORRs increase by 13.7-59.0%

629   to 0.62-0.87. Overall, the biases at the independent sites are similar or slightly worse

630   than those at the assimilated sites, which is reasonable since the closer to the assimilated

631   site the independent sites are, the more constraints of observation information can be

632   obtained, and the improvements in optimized state variables of the model are more

633   significant. For example, generally, the transmission distance of NO_2 is relatively short,

634   and remote cities with small emission correlations to the cities with assimilated

635   observations are relatively less constrained, resulting in only a 26.7% decrease in the

636   RMSE.
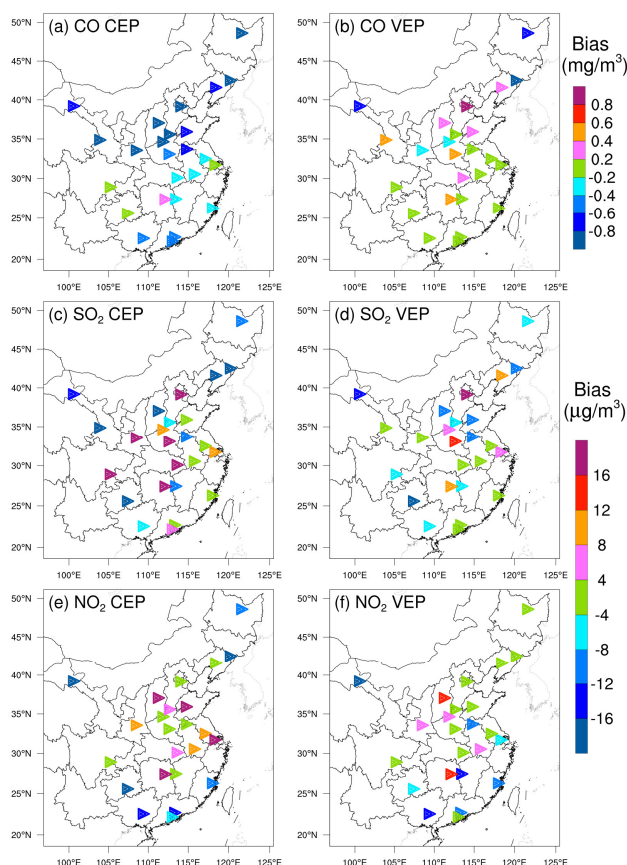
637

638   **Figure 7**. As in Fig. 5 but for the independent validation.
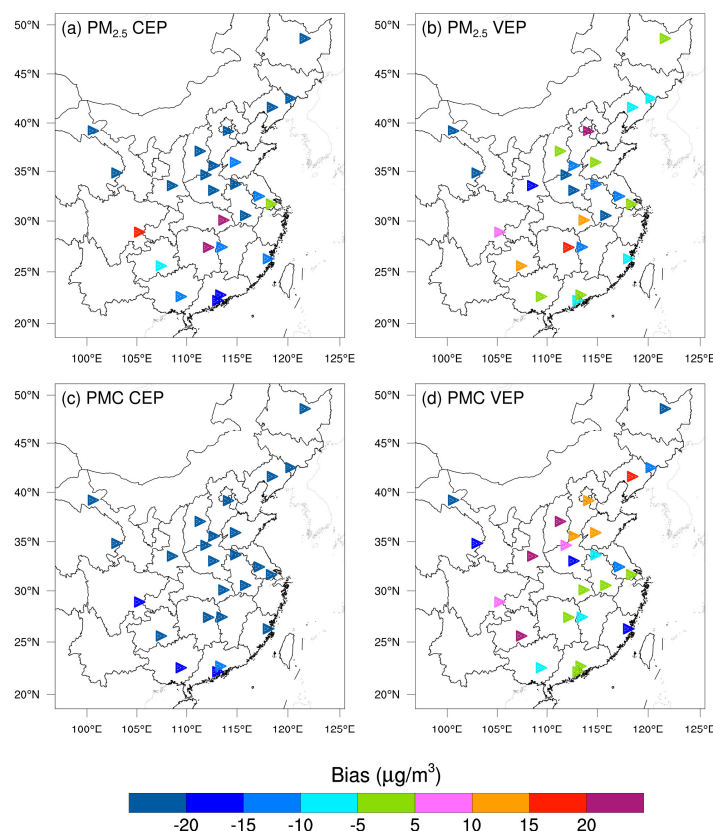
Figure 8. As in Fig. 6 but for the independent validation.

Compared with the previous studies, Tang et al. (2013) conducted inversion of CO emissions over Beijing and the surrounding areas, the improvements (Table 6) in the RMSE (37-48% vs. 30-51%) and the CORR (both studies ~ 0.81) are comparable, but the biases here could decrease by 90-97%, which is much greater than their 48-64% reductions. Additionally, Chen et al. (2019) showed that the RMSE of simulated SO_2 with updated SO_2 emissions decreased by 4.2-52.2% for different regions, and the CORR only increased to 0.69 at most. The improvement is relatively smaller than our results, which may be due to the insufficient adjustment of emissions caused by the underestimated ensemble spread through the inflation method. The better performance in this study may be related to our inversion process that makes the optimized emissions

32

651   of the current DA window propagate to the next DA window for further correction.

652   **Table 6**. Statistics comparing the pollution concentrations from the simulations with

653   prior (CEP) and posterior (VEP) emissions against assimilated and independent

654   observations, respectively. CO unit: mg m^{-3}; others units: µg m^{-3}.

Species	Mean Obs.	Mean Sim.		BIAS		RMSE		CORR	
		CEP	VEP	CEP	VEP	CEP	VEP	CEP	VEP
Against assimilated observations									
CO	1.43	0.66	1.36	-0.77	-0.08	1.08	0.56	0.46	0.81
SO$_2$	32.5	34.4	28.4	1.9	-4.1	42.4	17.7	0.39	0.88
NO$_2$	43.8	40.8	39.0	-2.9	-4.8	25.0	12.3	0.65	0.88
PM$_{2.5}$	77.0	53.1	70.3	-24.0	-6.7	50.3	29.6	0.64	0.87
PMC	40.5	8.1	37.5	-32.4	-3.1	41.5	24.6	0.25	0.69
Against independent observations									
CO	1.54	0.79	1.52	-0.75	-0.02	1.15	0.72	0.59	0.82
SO$_2$	40.6	39.2	37.3	-1.3	-3.2	44.3	27.2	0.57	0.87
NO$_2$	50.2	50.0	47.5	-0.3	-2.7	21.7	15.9	0.73	0.83
PM$_{2.5}$	91.5	64.6	84.1	-26.9	-7.4	64.1	37.2	0.62	0.87
PMC	42.0	9.2	40.4	-32.8	-1.6	39.3	26.6	0.39	0.62

655   * BIAS, mean bias; RMSE, root mean square error; CORR, correlation coefficient

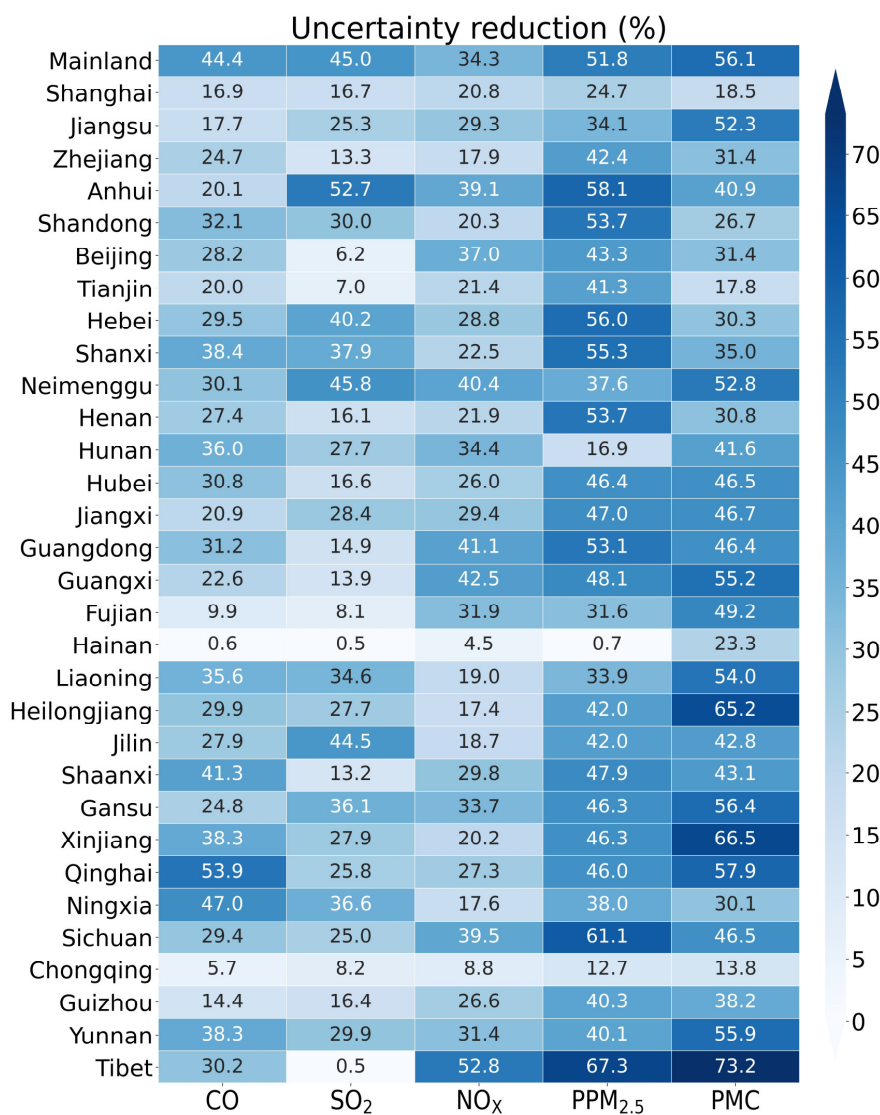656   **4.1.4 Uncertainty reduction**

657   The uncertainty reduction rate (UR) is another important quantity to evaluate the

658   performance of RAPAS and the effectiveness of in-situ observations in this system

659   (Chevallier et al., 2007; Jiang et al., 2021; Takagi et al., 2011). Following Jiang et al.

660   (2021), the UR is calculated as

661
$$UR = (1 - \frac{\sigma_{posterior}}{\sigma_{prior}}) \times 100 \qquad (19)$$

662   where $\sigma_{posterior}$ and σ_{prior} are the posterior and prior uncertainties, respectively.

663   Figure 9 shows the URs averaged in each province and the whole mainland China. The

664   URs vary with species, and among the 5 species of emissions, the uncertainties of the

665   PPM$_{2.5}$ and PMC are greatly reduced, while the UR of NO$_x$ emission is lowest, that is

666   because the URs are closely related to the magnitude settings of prior uncertainties

667   (Jiang et al., 2021). For the whole mainland China, the uncertainties are reduced by

668 44.4%, 45.0%, 34.3%, 51.8% and 56.1% for CO, SO_2, NO_x, $PPM_{2.5}$ and PMC,

669 respectively. For one species, it also varies across provinces. The URs are usually

670 related to observation coverage, which means that the more observation constraints

671 there are, the more the URs decrease. Additionally, the URs may also relate to emission

672 distributions. Generally, the URs are more significant in the provinces where the

673 observations and emissions are both relatively concentrated (e.g., Tibet), while they are

674 much lower in where the emissions are scattered or relatively uniform, but the

675 observations are only in large cities, even though there are many more observations

676 than other provinces.

Uncertainty reduction (%)

	CO	SO$_2$	NO$_X$	PPM$_{2.5}$	PMC
Mainland	44.4	45.0	34.3	51.8	56.1
Shanghai	16.9	16.7	20.8	24.7	18.5
Jiangsu	17.7	25.3	29.3	34.1	52.3
Zhejiang	24.7	13.3	17.9	42.4	31.4
Anhui	20.1	52.7	39.1	58.1	40.9
Shandong	32.1	30.0	20.3	53.7	26.7
Beijing	28.2	6.2	37.0	43.3	31.4
Tianjin	20.0	7.0	21.4	41.3	17.8
Hebei	29.5	40.2	28.8	56.0	30.3
Shanxi	38.4	37.9	22.5	55.3	35.0
Neimenggu	30.1	45.8	40.4	37.6	52.8
Henan	27.4	16.1	21.9	53.7	30.8
Hunan	36.0	27.7	34.4	16.9	41.6
Hubei	30.8	16.6	26.0	46.4	46.5
Jiangxi	20.9	28.4	29.4	47.0	46.7
Guangdong	31.2	14.9	41.1	53.1	46.4
Guangxi	22.6	13.9	42.5	48.1	55.2
Fujian	9.9	8.1	31.9	31.6	49.2
Hainan	0.6	0.5	4.5	0.7	23.3
Liaoning	35.6	34.6	19.0	33.9	54.0
Heilongjiang	29.9	27.7	17.4	42.0	65.2
Jilin	27.9	44.5	18.7	42.0	42.8
Shaanxi	41.3	13.2	29.8	47.9	43.1
Gansu	24.8	36.1	33.7	46.3	56.4
Xinjiang	38.3	27.9	20.2	46.3	66.5
Qinghai	53.9	25.8	27.3	46.0	57.9
Ningxia	47.0	36.6	17.6	38.0	30.1
Sichuan	29.4	25.0	39.5	61.1	46.5
Chongqing	5.7	8.2	8.8	12.7	13.8
Guizhou	14.4	16.4	26.6	40.3	38.2
Yunnan	38.3	29.9	31.4	40.1	55.9
Tibet	30.2	0.5	52.8	67.3	73.2

Figure 9. Time-averaged posterior emission uncertainty reduction (%) indicated by the standard deviation reduction of total emissions per province calculated by prior and posterior ensembles.

4.2 Inverted emissions
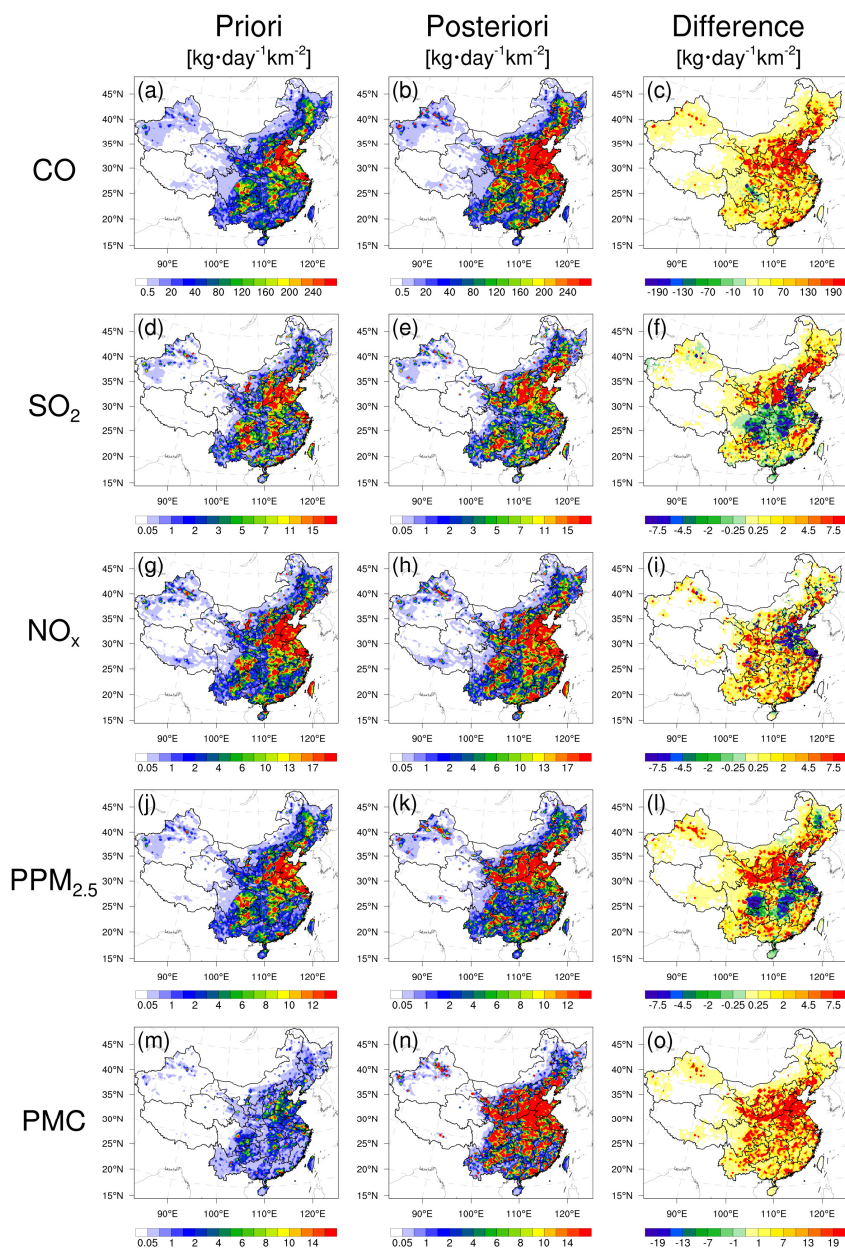
Figure 10 shows the spatial distribution of the temporal averaged prior and posterior emissions and their differences. Higher emissions are mainly concentrated in central

684 and eastern China, especially in the NCP, YRD, and PRD, and lower emissions occur

685 across Northwest and Southern China. Compared with the prior emissions, posterior

686 CO emissions are considerably increased across most areas of mainland China,

687 especially in northern China, with an overall increase of 129%. Notable

688 underestimation of the prior emissions is also confirmed by previous inversion

689 estimations (Feng et al., 2020b; Tang et al., 2013; Wu et al., 2020) and model

690 evaluations (Kong et al., 2019a). For SO_2, the emission increases mainly occur in

691 Northeast China, Shanxi, Ningxia, Gansu, Fujian, Jiangxi and Yunnan provinces. In

692 SCB, Central China, YRD, and part of NCP, the emissions are significantly reduced.

693 For national total, the SO_2 emission is increased by 20%. For NO_x, although the

694 increment of national total emissions is small, only about 5%, large deviations still exist

695 on regional scale. Obviously, the emissions in the NCP and YRD are reduced, while in

696 the other regions, the emissions of most cities are increased. The changes in $PPM_{2.5}$

697 emission are similar to SO_2. Compared with the prior emission, the posterior $PPM_{2.5}$

698 emissions are decreased over central China, SCB and YRD, while the ones in southern

699 and northern China are increased, especially in Shanxi, Shaanxi, Gansu and southern

700 Hebei province. Overall, the relative increase is 95%. For PMC, the posterior emissions

701 are increased over the whole mainland China, with national mean relative increase

702 exceeding 1000%. Larger emission increments mainly occur in the areas where have

703 significant anthropogenic emissions of CO and $PPM_{2.5}$, indicating that the large

704 underestimations of PMC emissions in the prior inventory may be mainly attributed to

705 the underestimations of anthropogenic activities. In addition, without dust may be

706 another reason, since no wind blowing dust scheme was applied in this study as

707 mentioned above. Large PMC emission increment are also found in Ma et al (2019).

708 Detailed estimation of posterior emissions and relative changes compared to prior

709 emissions in each province and the whole mainland China is given in Table S1. Note

710 that the differences, excluding PMC, between the prior and posterior emissions mainly

711 reflect the deficiencies of the prior emissions because the times of the prior emissions

712 and the observations are completely consistent in this study.

Figure 10. Spatial distribution of the time-averaged prior emissions (left column, MEIC 2016), posterior emissions (middle column), and differences (right column, posterior minus prior).

4.3 Sensitivity tests

4.3.1 The advantages of "two-step" scheme

Adjusting the ICs and emissions simultaneously (i.e., "one-step" scheme) has been applied to constrain prior emissions in many previous studies (Evensen, 2009; Kong et al., 2019b). To investigate the impact of different methods on the optimized emissions, a sensitivity test (EMS1) is performed, in which the initial fields of each DA window are optimized using the 3DVAR algorithm directly. Compared with our "two-step" method (EMDA), the posterior emissions of EMS1 are increased by 7%, 1.4%, 0.6%, 22.2%, and 17.2% for CO, SO_2, NO_x, $PM_{2.5}$ and PMC, respectively. As mentioned previously, in the "two-step" scheme, the optimized emission can be sufficiently fed back to the concentration field and fully mixed in the atmosphere (1 day), and the error transfer makes the system consistently and stably updated. If the emission in one window is overestimated, in this way, it could be compensated in the next window with lower estimates. In contrast, when initial fields assimilating with observations simultaneously at each window, the overestimation will not be corrected and will accumulate to the end. We also evaluate the posterior emissions of EMS1 using the same method as shown in Sect. 4.1.3. Figure 11 shows the time series of simulated and observed daily concentrations and their RMSEs verified against the assimilated sites. Overall, compared to the base experiment (EMDA), the performance of EMS1 is significantly worse, with RMSEs of CO, SO_2, NO_2, $PM_{2.5}$ and PMC increasing from 0.56 mg m^{-3}, 17.7, 12.3, 29.6, and 24.6 μg m^{-3} to 0.69 mg m^{-3}, 18.8, 13.3, 36.8, and 33.3 μg m^{-3}, respectively. Additionally, it can be seen from the figure that the results of the two experiments are relatively close at the beginning and during the heavy pollution period (16-21 December). However, after that, the simulated results with "one-step" inversion emissions are significantly higher than the observations, and these large biases continue until the end. The results verified against the independent sites also show a similar situation (Fig. S2). The reason may be that during the period of heavy pollution, the WRF-CMAQ (off-line model) does not consider the feedback process of meteorology and chemistry, resulting in low simulations. Therefore, the system will

746 compensate for the underestimated concentrations caused by the model error through

747 more emissions, resulting in the overestimation of emissions. The accumulation of

748 emission error in each independent window further leads to the overestimation of

749 concentration after the end of high pollution, especially for species with a long lifetime

750 (e.g., CO). On the contrary, this overestimation will be corrected quickly in the

751 subsequent inversion using the "two-step" inversion scheme in this study, so as to

752 ensure the stability of the system. It should be noted that the model performance

753 depends on many factors but does not affect the advantage of the "two-step" scheme.
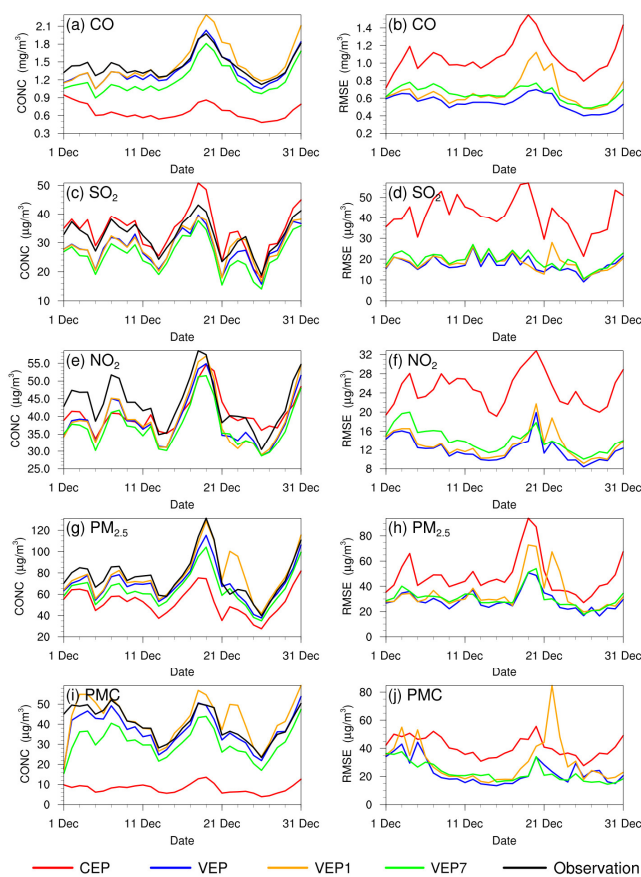

754

755 **Figure 11**. Time series of the daily concentrations (CONC, left) and root mean square

756 error (RMSE, right) obtained from CEP, VEP, VEP1, and VEP3. The simulations were

757 verified against the assimilated sites.

4.3.2 Impact of prior inventories

Various prior inventories have great differences in space allocation and emission magnitude. Inversion results can be sensitive to a priori emissions if the observation is insufficient (Gurney et al., 2004; He et al., 2018). MEIC 2012 is used as an alternative a priori in EMS2 to investigate the impact of different prior emissions on the posteriori. Figure 12 shows the time series of the relative differences in daily posterior emissions of the five species between the EMDA (base) and EMS2 experiments. Overall, the differences between the two posterior emissions gradually decrease over time. At the beginning, the differences in the CO, SO_2, NO_x, $PPM_{2.5}$ and PMC between the two inventories (i.e., MEIC 2012 vs MEIC 2016) are 17.5%, 114.5%, 30.8%, 46.0% and 72.0%, respectively, while during the last ten days, the differences of the two posterior emissions have decreased to 2.5%, 4.5%, 4.5%, -8.9% and 3.0%, respectively. In addition, it also could be found that the species that has larger emission differences at the beginning take a longer time (namely more DA steps) to achieve convergence. The quick convergence of PMC emission is attributed to the large prior uncertainty of 100% used in the first 3 DA windows. Different from the other species, there are significant negative deviations of $PPM_{2.5}$ emissions between the two experiments. That may be due to the positive deviations in the precursors of $PM_{2.5}$ (i.e., SO_2 and NO_x), which will lead to a larger amount of secondary production. To balance the total $PM_{2.5}$ concentration, the $PPM_{2.5}$ emissions will be reduced. We compare the $PM_{2.5}$ concentrations simulated by the two optimized inventories and find that they are almost the same (Fig. S3). Overall, this indicates that the observation in China is sufficient in inferring the emissions, and our system is rather robust. Meanwhile, it also suggests that the monthly posterior emissions shown in Sect. 4.2 are still underestimated to a certain extent.
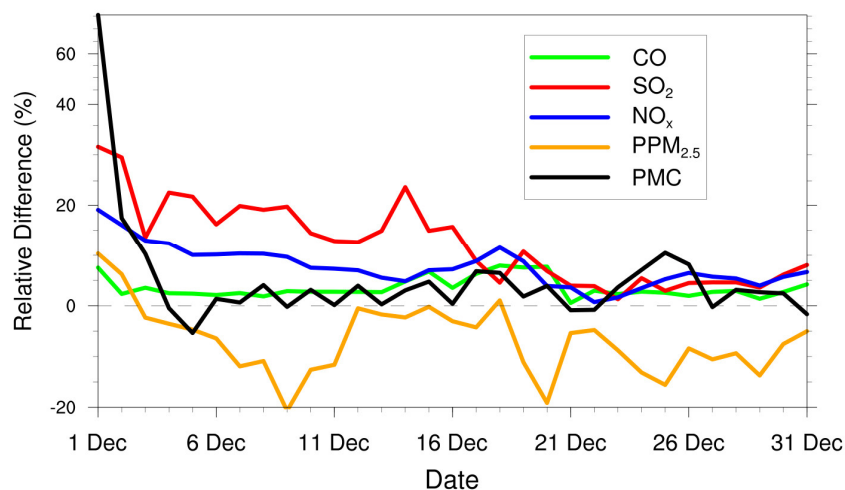
Figure 12. Relative differences in CO, SO_2, NO_x, $PPM_{2.5}$ and PMC emissions (%, the ratio of absolute difference to EMDA) between the EMDA and EMS2 experiments.

4.3.3 Impact of prior uncertainties settings

The uncertainty of prior emissions determines how closely the analysis is weighted toward the background and observation, but information about prior uncertainties is generally not readily available. To evaluate the possible influence of prior uncertainties on the optimized emissions, we increased/reduced the uncertainties after 3 days of cycling, namely starting at 0000 UTC, 3 December, by 25% and 50 % in EMS3 (-50%), EMS4 (-25%), EMS5 (+25%) and EMS6 (+50%), respectively. Table 7 summarizes the emission changes with different prior uncertainties settings in EMS3-6 experiments. To better understand the response of the system to the emission uncertainty settings, Fig. 13 shows the time series of SO_2 emission changes and the RMSEs of simulated SO_2 with emissions updated in the EMDA and EMS3-6 experiments over the YRD and NCP (Fig. 2). Compared with the EMDA, when the uncertainties are decreased (increased), the emissions of the 5 species decrease (increase) accordingly. That is because the posterior emissions of the 5 species are larger than the prior emissions, and as shown in Fig. 13, larger uncertainty will lead to a faster convergence, resulting in larger

Geoscientific
Model Development
Discussions

802　posterior emissions. It also could be found from Fig. 13 that a faster convergence will

803　indeed reduce the RMSE of the simulated concentration with the posterior emissions in

804　the early stage of the experiment, but in the later stage of the experiment, there are no

805　significant differences for the RMSE among the different experiments. In addition, it

806　shows that when greater uncertainties are set, the day-to-day changes in emissions are

807　also more drastic, resulting in a larger RMSE as shown in NCP. Moreover, those

808　significant day-to-day variations of estimated emissions may not be in line with the

809　actual situation. Overall, the uncertainties chosen in EMDA aim to minimize the

810　deviation of the concentration fields and maintain the stability of inversion.

811　**Table 7**. Relative differences in CO, SO_2, NO_x, $PPM_{2.5}$ and PMC emissions (%, the

812　ratio of absolute difference to EMDA) between the EMDA and EMS3-6 experiments.

Species	EMS3	EMS4	EMS5	EMS6
CO	-8.6	-4	3	5.2
SO_2	-14	-5.7	3.6	6.8
NO_x	-6.5	-3	2.8	4.5
$PPM_{2.5}$	-16.5	-7.8	4.6	8.7
PMC	-18.5	-8.2	7.3	13.1

813

814
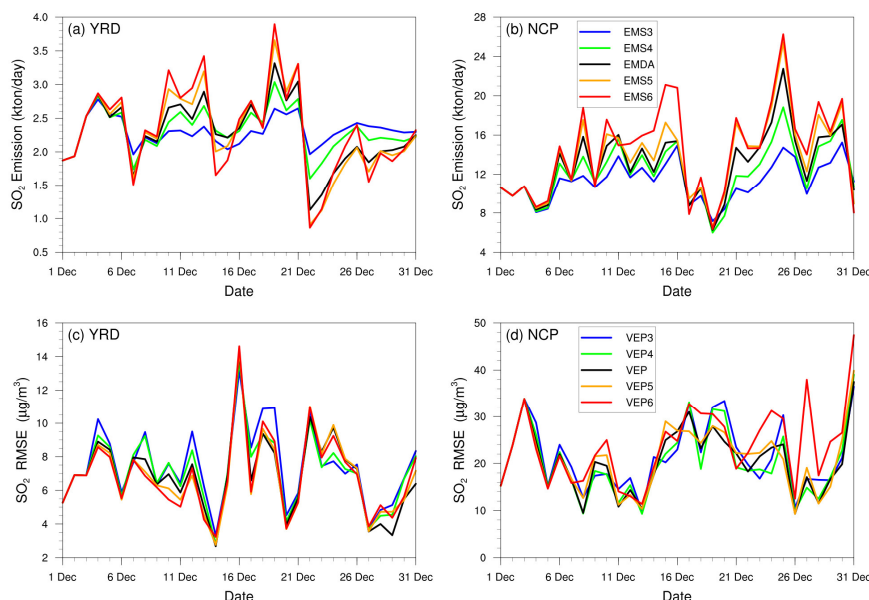
Figure 13. Time-series of SO_2 emissions changes and the RMSE of simulated SO_2 with
updated SO_2 emissions in the EMDA and EMS3-6 experiments over the Yangtze River
Delta (YRD) and North China Plain (NCP).

4.3.4 Impact of observation error settings

Another factor that determines the relative weights of the observation and background
in the analysis is observation errors. A proper estimate of the observation error is also
important in regard to the filter performance, but observation errors are not provided
with the dataset. The observation error is usually set to a fixed value (Ma et al., 2019),
a specific proportion of the observation value (Tang et al., 2013) or the value calculated
by combining measurement error with representative error as used in this study.
Generally, the performance of the data assimilation is quite sensitive to the specification
of observation error (Tang et al., 2013). To evaluate the influence of observation error
on the optimized emissions, a sensitivity experiment (EMS7) with doubled observation
error was conducted. Overall, the spatial distribution of emissions after optimization is
almost the same as that of the EMDA experiment, but the increment is lower (Fig. S4),

830 resulting in a weaker estimate of the national total emission for each species. That is

831 because that the observation error becomes large, the system will be more convinced of

832 the prior emission and reduce the effect of observation information. The simulations in

833 VEP7 usually perform worse, with larger biases and RMSEs than those of VEP (Figs

834 11, S2 and S5), especially in most of western and southern China where posterior

835 emissions are still significantly underestimated, suggesting that too large observation

836 error may substantially impact the estimated emissions.

837 **5 Summary and conclusions**

838 In this study, we developed a Regional multi-Air Pollutant Assimilation System

839 (RAPASv1.0) based on the WRF/CMAQ model, 3DVAR and EnKF algorithm. RAPAS

840 can quantitatively optimize gridded emissions of CO, SO_2, NO_x, $PPM_{2.5}$ and PMC on

841 regional scale by simultaneously assimilating hourly in-situ measurements of CO, SO_2,

842 NO_2, $PM_{2.5}$ and PM_{10}. This system includes two subsystems, namely the IA subsystem

843 and the EI subsystem, which optimizes the chemical ICs, and infers the anthropogenic

844 emissions, respectively.

845 Taking the 2016 Multi-resolution Emission Inventory for China (MEIC 2016) in

846 December as a priori, the emissions of CO, SO_2, NO_x, $PPM_{2.5}$ and PMC in December

847 2016 were inferred through assimilating the corresponding nationwide observations

848 over China. The optimized ICs and posterior emissions were examined against the

849 assimilated and independent observations through parallel forward simulation

850 experiments with and without DA. Sensitivity tests are also performed to investigate

851 the impact of different inversion processes, prior emissions, prior uncertainties and

852 observation errors on the emission estimates.

853 The results show that RAPAS can significantly improve the simulations and reduce the

854 uncertainties of the emissions. For the whole mainland China, the emission

855 uncertainties reduced by 44.4%, 45.0%, 34.3%, 51.8% and 56.1% for CO, SO_2, NO_x,

856 $PPM_{2.5}$ and PMC, respectively, the RMSEs of the simulated concentrations with

857 posterior emissions decreased by 40.1-56.3%, and the CORRs increased from 0.26-0.66

858   to 0.69-0.87 for different species. Overall, compared with the prior emissions (MEIC

859   2016), the posterior emissions increased by 129%, 20%, 5% and 95% for CO, SO_2, NO_x

860   and $PPM_{2.5}$, respectively. The posterior PMC emissions, which included anthropogenic

861   and natural dust contributions, increased by 1045%. The sensitivity tests with different

862   inversion processes show that the "two-step" scheme in emission inversion outperforms

863   the joint adjustment of ICs and emissions ("one-step" scheme), especially after heavy

864   pollution. The sensitivity tests with different prior inventories show the observation in

865   China is sufficient in inferring the emissions, and our system is less dependent on prior

866   inventories. Additionally, the sensitivity tests with different prior uncertainties indicate

867   that when the posterior emissions are larger than the prior emissions, the emissions

868   decrease/increase with the decreases/increases of uncertainties because of the different

869   convergence rates. These results demonstrate the advantage of the two-step method in

870   emission inversion in that the inversion errors of the last window could be transferred

871   to the current window for further optimization and the robustness of the emissions

872   estimated from RAPAS using the nationwide observations over China. It should be

873   noted that the system usually responds slowly to too small a priori uncertainty or too

874   large observation error, which may result in large errors in the estimated emissions.

875   Independent variable localization was adopted to avoid potential spurious correlations

876   across different species in this study. However, the transmission scales for different

877   species in different regions are still different, and a more accurate localization range

878   could be obtained through backward trajectory analysis. In additionally, O_3

879   observations are not assimilated to improve NO_x and VOC emissions using cross-

880   species information due to the strong nonlinear effects within the O_3-NO_x-VOC

881   relationship, in which the O_3 concentration and NO_x (VOC) emissions are positively

882   correlated in the NO_x (VOC)-limited region and negatively correlated in the VOC

883   (NO_x)-limited region (Tang et al., 2011). This work will be followed up by an ongoing

884   work using available VOC observations. As shown previously, the concentrations after

885   DA are obviously underestimated in western China, indicating that the inverted

886   emissions over these regions still have large uncertainties because of the sparsity of

Geoscientific
Model Development
Discussions

887 observations that are spatially insufficient for sampling the inhomogeneity of emissions.

888 Therefore, further investigations with joint assimilation of multisource observations

889 (e.g., satellite) are also underway.

890 In summary, this study offers a useful tool for accurately quantifying multi-species

891 anthropogenic emissions at large scales and near-real time, which will serve better for

892 monitoring emission changes and designing future emissions regulations and pollution

893 control.

894

895 **Code and data availability**

896 The WRF model code is open-source code and can be obtained from the WRF Model

897 User's Page (https://www2.mmm.ucar.edu/wrf/users, last access: 25 April 2021). The

898 CMAQ model is available through an open license as well (https://www.epa.gov/cmaq ,

899 last access: 25 April 2021). The observation and emission data used in this paper are

900 available at https://doi.org/10.5281/zenodo.4718290 (Feng and Jiang, 2021). The code

901 of this system can be obtained on request from the corresponding author

902 (jiangf@nju.edu.cn).

903

904 **Author contribution**

905 SF, FJ, ZW and ZJ developed RAPAS v1.0. SF and FJ designed the research. SF

906 performed model simulations, analyzed data, and prepared the paper with contributions

907 from all co-authors. FJ supervised the model development project and assisted in

908 conceptualization and writing. HW, WH, YS, LZ, YZ, CL, and WJ contributed to the

909 discussion and improvement of the paper.

910

911 **Competing interests**

912 The authors declare that they have no conflict of interest.

922 **References**

923 Appel, K. W., Pouliot, G. A., Simon, H., Sarwar, G., Pye, H. O. T., Napelenok, S. L., Akhtar, F., and
924   Roselle, S. J.: Evaluation of dust and trace metal estimates from the Community Multiscale Air
925   Quality (CMAQ) model version 5.0, Geoscientific Model Development, 6, 883-899,
926   10.5194/gmd-6-883-2013, 2013.

927 Bauwens, M., Compernolle, S., Stavrakou, T., Müller, J.-F., van Gent, J., Eskes, H., Levelt, P. F.,
928   van der A, R., Veefkind, J. P., Vlietinck, J., Yu, H., and Zehner, C.: Impact of Coronavirus
929   Outbreak on NO2 Pollution Assessed Using TROPOMI and OMI Observations, 47,
930   e2020GL087978, 10.1029/2020gl087978, 2020.

931 Binkowski, F. S. and Roselle, S. J.: Models-3 community multiscale air quality (CMAQ) model
932   aerosol component - 1. Model description, Journal of Geophysical Research-Atmospheres, 108,
933   10.1029/2001jd001409, 2003.

934 Bruhwiler, L. M. P., Michalak, A. M., Peters, W., Baker, D. F., and Tans, P.: An improved Kalman
935   Smoother for atmospheric inversions, Atmos. Chem. Phys., 5, 2691-2702, 10.5194/acp-5-2691-
936   2005, 2005.

937 Chen, D., Liu, Z., Ban, J., and Chen, M.: The 2015 and 2016 wintertime air pollution in China: SO2
938   emission changes derived from a WRF-Chem/EnKF coupled data assimilation system,
939   Atmospheric Chemistry and Physics, 19, 8619-8650, 10.5194/acp-19-8619-2019, 2019.

940 Chen, D., Liu, Z., Fast, J., and Ban, J.: Simulations of sulfate-nitrate-ammonium (SNA) aerosols
941   during the extreme haze events over northern China in October 2014, Atmospheric Chemistry
942   and Physics, 16, 10707-10724, 10.5194/acp-16-10707-2016, 2016.

943 Chevallier, F., Bréon, F.-M., and Rayner, P. J.: Contribution of the Orbiting Carbon Observatory to
944   the estimation of CO2 sources and sinks: Theoretical study in a variational data assimilation
945   framework, 112, 10.1029/2006JD007375, 2007.

946 Clements, A. L., Fraser, M. P., Upadhyay, N., Herckes, P., Sundblom, M., Lantz, J., and Solomon,
947   P. A.: Chemical characterization of coarse particulate matter in the Desert Southwest - Pinal
948   County Arizona, USA, Atmospheric Pollution Research, 5, 52-61, 10.5094/apr.2014.007, 2014.

949 Clements, N., Hannigan, M. P., Miller, S. L., Peel, J. L., and Milford, J. B.: Comparisons of urban
950   and rural PM10-2.5 and PM2.5 mass concentrations and semi-volatile fractions in northeastern

951   Colorado, Atmospheric Chemistry and Physics, 16, 7469-7484, 10.5194/acp-16-7469-2016, 2016.

952   de Foy, B., Lu, Z., Streets, D. G., Lamsal, L. N., and Duncan, B. N.: Estimates of power plant NOx
953   emissions and lifetimes from OMI NO2 satellite retrievals, Atmospheric Environment, 116, 1-11,
954   10.1016/j.atmosenv.2015.05.056, 2015.

955   Descombes, G., Auligne, T., Vandenberghe, F., Barker, D. M., and Barre, J.: Generalized
956   background error covariance matrix model (GEN_BE v2.0), Geoscientific Model Development,
957   8, 669-696, 10.5194/gmd-8-669-2015, 2015.

958   Ding, J., van der A, R. J., Mijling, B., Levelt, P. F., and Hao, N.: NOx emission estimates during the
959   2014 Youth Olympic Games in Nanjing, Atmospheric Chemistry and Physics, 15, 9399-9412,
960   10.5194/acp-15-9399-2015, 2015.

961   Elbern, H., Strunk, A., Schmidt, H., and Talagrand, O.: Emission rate and chemical state estimation
962   by 4-dimensional variational inversion, Atmospheric Chemistry and Physics, 7, 3749-3769,
963   10.5194/acp-7-3749-2007, 2007.

964   Evensen, G.: The Ensemble Kalman Filter for Combined State and Parameter Estimation MONTE
965   CARLO TECHNIQUES FOR DATA ASSIMILATION IN LARGE SYSTEMS, Ieee Control
966   Systems Magazine, 29, 83-104, 10.1109/mcs.2009.932223, 2009.

967   Feng, S., Jiang, F., Jiang, Z., Wang, H., Cai, Z., and Zhang, L.: Impact of 3DVAR assimilation of
968   surface PM2.5 observations on PM2.5 forecasts over China during wintertime, Atmospheric
969   Environment, 187, 34-49, 10.1016/j.atmosenv.2018.05.049, 2018.

970   Feng, S., Jiang, F., Wu, Z., Wang, H., Ju, W., and Wang, H.: CO Emissions Inferred From Surface
971   CO Observations Over China in December 2013 and 2017, Journal of Geophysical Research-
972   Atmospheres, 125, 10.1029/2019jd031808, 2020a.

973   Feng, S., Jiang, F., Wang, H., Wang, H., Ju, W., Shen, Y., Zheng, Y., Wu, Z., and Ding, A.: NOx
974   Emission Changes Over China During the COVID-19 Epidemic Inferred From Surface NO2
975   Observations, Geophysical Research Letters, 47, 10.1029/2020gl090080, 2020b.

976   Feng, S. and Jiang, F.: Anthropogenic air pollutant emissions over China inferred by Regional multi-
977   Air Pollutant Assimilation System (RAPAS v1.0), Zenodo, 10.5281/zenodo.4718290, 2021.

978   Gaspari, G. and Cohn, S. E.: Construction of correlation functions in two and three dimensions,
979   Quarterly Journal of the Royal Meteorological Society, 125, 723-757, 10.1256/smsqj.55416, 1999.

980   Guenther, A. B., Jiang, X., Heald, C. L., Sakulyanontvittaya, T., Duhl, T., Emmons, L. K., and Wang,
981   X.: The Model of Emissions of Gases and Aerosols from Nature version 2.1 (MEGAN2.1): an
982   extended and updated framework for modeling biogenic emissions, Geoscientific Model
983   Development, 5, 1471-1492, 10.5194/gmd-5-1471-2012, 2012.

984   Gurney, K. R., Law, R. M., Denning, A. S., Rayner, P. J., Pak, B. C., Baker, D., Bousquet, P.,
985   Bruhwiler, L., Chen, Y. H., Ciais, P., Fung, I. Y., Heimann, M., John, J., Maki, T., Maksyutov, S.,
986   Peylin, P., Prather, M., and Taguchi, S.: Transcom 3 inversion intercomparison: Model mean
987   results for the estimation of seasonal carbon sources and sinks, Global Biogeochemical Cycles,
988   18, 10.1029/2003gb002111, 2004.

989   He, W., van der Velde, I. R., Andrews, A. E., Sweeney, C., Miller, J., Tans, P., van der Laan-Luijkx,
990   I. T., Nehrkorn, T., Mountain, M., Ju, W., Peters, W., and Chen, H.: CTDAS-Lagrange v1.0: a
991   high-resolution data assimilation system for regional carbon dioxide observations, Geoscientific
992   Model Development, 11, 3515-3536, 10.5194/gmd-11-3515-2018, 2018.

993   Hinds, W.C.: Aerosol Technology: Properties, Behavior, and Measurement of Airborne Particles.
994   New York: John Wiley, 1982.

995   Houtekamer, P. L. and Mitchell, H. L.: A sequential ensemble Kalman filter for atmospheric data
996   assimilation, Monthly Weather Review, 129, 123-137, 10.1175/1520-
997   0493(2001)129<0123:asekff>2.0.co;2, 2001.

998   Houtekamer, P. L. and Zhang, F.: Review of the Ensemble Kalman Filter for Atmospheric Data
999   Assimilation, Monthly Weather Review, 144, 4489-4532, 10.1175/mwr-d-15-0440.1, 2016.

1000 Jiang, F., Liu, Q., Huang, X., Wang, T., Zhuang, B., and Xie, M.: Regional modeling of secondary
1001   organic aerosol over China using WRF/Chem, Journal of Aerosol Science, 43, 57-73,
1002   10.1016/j.jaerosci.2011.09.003, 2012a.

1003 Jiang, F., Zhou, P., Liu, Q., Wang, T., Zhuang, B., and Wang, X.: Modeling tropospheric ozone
1004   formation over East China in springtime, Journal of Atmospheric Chemistry, 69, 303-319,
1005   10.1007/s10874-012-9244-3, 2012b.

1006 Jiang, F., Wang, H. M., Chen, J. M., Machida, T., Zhou, L. X., Ju, W. M., Matsueda, H., and Sawa,
1007   Y.: Carbon balance of China constrained by CONTRAIL aircraft CO2 measurements,
1008   Atmospheric Chemistry and Physics, 14, 10133-10144, 10.5194/acp-14-10133-2014, 2014.

1009 Jiang, F., Wang, H., Chen, J. M., Ju, W., Tian, X., Feng, S., Li, G., Chen, Z., Zhang, S., Lu, X., Liu,
1010   J., Wang, H., Wang, J., He, W., and Wu, M.: Regional CO2 fluxes from 2010 to 2015 inferred
1011   from GOSAT XCO2 retrievals using a new version of the Global Carbon Assimilation System,
1012   Atmos. Chem. Phys., 21, 1963-1985, 10.5194/acp-21-1963-2021, 2021.

1013 Jiang, W., Smyth, S., Giroux, E., Roth, H., and Yin, D.: Differences between CMAQ fine mode
1014   particle and PM2.5 concentrations and their impact on model performance evaluation in the lower
1015   Fraser valley, Atmospheric Environment, 40, 4973-4985, 10.1016/j.atmosenv.2005.10.069, 2006.

1016 Jiang, Z., Liu, Z., Wang, T., Schwartz, C. S., Lin, H.-C., and Jiang, F.: Probing into the impact of
1017   3DVAR assimilation of surface PM10 observations over China using process analysis, Journal of
1018   Geophysical Research: Atmospheres, 118, 6738-6749, 10.1002/jgrd.50495, 2013.

1019 Jiang, Z., Worden, J. R., Worden, H., Deeter, M., Jones, D. B. A., Arellano, A. F., and Henze, D. K.:
1020   A 15-year record of CO emissions constrained by MOPITT CO observations, Atmospheric
1021   Chemistry And Physics, 17, 4565-4583, 10.5194/acp-17-4565-2017, 2017.

1022 Jin, J., Lin, H. X., Heemink, A., and Segers, A.: Spatially varying parameter estimation for dust
1023   emissions using reduced-tangent-linearization 4DVar, Atmospheric Environment, 187, 358-373,
1024   10.1016/j.atmosenv.2018.05.060, 2018.

1025 Kang, J.-S., Kalnay, E., Miyoshi, T., Liu, J., and Fung, I.: Estimation of surface carbon fluxes with
1026   an advanced data assimilation methodology, 117, 10.1029/2012JD018259, 2012.

1027 Kleist, D. T., Parrish, D. F., Derber, J. C., Treadon, R., Wu, W.-S., and Lord, S.: Introduction of the
1028   GSI into the NCEP Global Data Assimilation System, Weather and Forecasting, 24, 1691-1705,
1029   10.1175/2009waf2222201.1, 2009.

1030 Kong, L., Tang, X., Zhu, J., Wang, Z., Pan, Y., Wu, H., Wu, L., Wu, Q., He, Y., Tian, S., Xie, Y., Liu,
1031   Z., Sui, W., Han, L., and Carmichael, G.: Improved Inversion of Monthly Ammonia Emissions in
1032   China Based on the Chinese Ammonia Monitoring Network and Ensemble Kalman Filter,
1033   Environmental Science & Technology, 53, 12529-12538, 10.1021/acsest.9b02701, 2019a.

1034 Kong, L., Tang, X., Zhu, J., Wang, Z., Fu, J. S., Wang, X., Itahashi, S., Yamaji, K., Nagashima, T.,

1035   Lee, H. J., Kim, C. H., Lin, C. Y., Chen, L., Zhang, M., Tao, Z., Li, J., Kajino, M., Liao, H., Sudo,
1036   K., Wang, Y., Pan, Y., Tang, G., Li, M., Wu, Q., Ge, B., and Carmichael, G. R.: Evaluation and
1037   uncertainty investigation of the NO2, CO and NH3 modeling over China under the framework of
1038   MICS-Asia III, Atmos. Chem. Phys. Discuss., 2019, 1-33, 10.5194/acp-2018-1158, 2019b.

1039   Kurokawa, J.-i., Yumimoto, K., Uno, I., and Ohara, T.: Adjoint inverse modeling of NOx emissions
1040   over eastern China using satellite observations of NO2 vertical column densities, Atmospheric
1041   Environment, 43, 1878-1887, 10.1016/j.atmosenv.2008.12.030, 2009.

1042   Li, M., Zhang, Q., Kurokawa, J.-i., Woo, J.-H., He, K., Lu, Z., Ohara, T., Song, Y., Streets, D. G.,
1043   Carmichael, G. R., Cheng, Y., Hong, C., Huo, H., Jiang, X., Kang, S., Liu, F., Su, H., and Zheng,
1044   B.: MIX: a mosaic Asian anthropogenic emission inventory under the international collaboration
1045   framework of the MICS-Asia and HTAP, Atmospheric Chemistry and Physics, 17, 935-963,
1046   10.5194/acp-17-935-2017, 2017.

1047   Liu, Z., Liu, Q., Lin, H.-C., Schwartz, C. S., Lee, Y.-H., and Wang, T.: Three-dimensional variational
1048   assimilation of MODIS aerosol optical depth: Implementation and application to a dust storm
1049   over East Asia, Journal of Geophysical Research: Atmospheres, 116, n/a-n/a,
1050   10.1029/2011jd016159, 2011.

1051   Ma, C., Wang, T., Mizzi, A. P., Anderson, J. L., Zhuang, B., Xie, M., and Wu, R.: Multiconstituent
1052   Data Assimilation With WRF-Chem/DART: Potential for Adjusting Anthropogenic Emissions
1053   and Improving Air Quality Forecasts Over Eastern China, 124, 7393-7412,
1054   10.1029/2019jd030421, 2019.

1055   Meirink, J. F., Eskes, H. J., and Goede, A. P. H.: Sensitivity analysis of methane emissions derived
1056   from SCIAMACHY observations through inverse modelling, Atmospheric Chemistry and
1057   Physics, 6, 1275-1292, 10.5194/acp-6-1275-2006, 2006.

1058   Miyazaki, K. and Eskes, H.: Constraints on surface NOx emissions by assimilating satellite
1059   observations of multiple species, Geophysical Research Letters, 40, 4745-4750,
1060   10.1002/grl.50894, 2013.

1061   Miyazaki, K., Eskes, H. J., and Sudo, K.: Global NOx emission estimates derived from an
1062   assimilation of OMI tropospheric NO2 columns, Atmospheric Chemistry and Physics, 12, 2263-
1063   2288, 10.5194/acp-12-2263-2012, 2012a.

1064   Miyazaki, K., Eskes, H. J., Sudo, K., Takigawa, M., van Weele, M., and Boersma, K. F.:
1065   Simultaneous assimilation of satellite NO2, O-3, CO, and HNO3 data for the analysis of
1066   tropospheric chemical composition and emissions, Atmospheric Chemistry and Physics, 12,
1067   9545-9579, 10.5194/acp-12-9545-2012, 2012b.

1068   Parrish, D. F. and Derber, J. C.: THE NATIONAL-METEOROLOGICAL-CENTERS SPECTRAL
1069   STATISTICAL-INTERPOLATION ANALYSIS SYSTEM, Monthly Weather Review, 120,
1070   1747-1763, 10.1175/1520-0493(1992)120<1747:tnmcss>2.0.co;2, 1992.

1071   Peng, Z., Liu, Z., Chen, D., and Ban, J.: Improving PM$_{2.5}$ forecast over
1072   China by the joint adjustment of initial conditions and source emissions with an ensemble Kalman
1073   filter, Atmospheric Chemistry and Physics, 17, 4837-4855, 10.5194/acp-17-4837-2017, 2017.

1074   Peng, Z., Lei, L., Liu, Z., Su, J., Ding, A., Ban, J., Chen, D., Kou, X., and Chu, K.: The impact of
1075   multi-species surface chemical observation assimilation on air quality forecasts in China,
1076   Atmospheric Chemistry and Physics, 18, 10.5194/acp-18-17387-2018, 2018.

Peters, W., Jacobson, A. R., Sweeney, C., Andrews, A. E., Conway, T. J., Masarie, K., Miller, J. B., Bruhwiler, L. M. P., Petron, G., Hirsch, A. I., Worthy, D. E. J., van der Werf, G. R., Randerson, J. T., Wennberg, P. O., Krol, M. C., and Tans, P. P.: An atmospheric perspective on North American carbon dioxide exchange: CarbonTracker, Proceedings of the National Academy of Sciences of the United States of America, 104, 18925-18930, 10.1073/pnas.0708986104, 2007.

Peylin, P., Rayner, P. J., Bousquet, P., Carouge, C., Hourdin, F., Heinrich, P., Ciais, P., and contributors, A.: Daily CO2 flux estimates over Europe from continuous atmospheric measurements: 1, inverse methodology, Atmospheric Chemistry and Physics, 5, 3173-3186, 10.5194/acp-5-3173-2005, 2005.

Purser, R. J., Wu, W. S., Parrish, D. F., and Roberts, N. M.: Numerical aspects of the application of recursive filters to variational statistical analysis. Part I: Spatially homogeneous and isotropic Gaussian covariances, Monthly Weather Review, 131, 1524-1535, 10.1175//1520-0493(2003)131<1524:naotao>2.0.co;2, 2003.

Rabier, F., McNally, A., Andersson, E., Courtier, P., Unden, P., Eyre, J., Hollingsworth, A., and Bouttier, F.: The ECMWF implementation of three-dimensional variational assimilation (3D-Var). II: Structure functions, Quarterly Journal Of the Royal Meteorological Society, 124, 1809-1829, 10.1256/smsqj.55002, 1998.

Sarwar, G., Simon, H., Bhave, P., and Yarwood, G.: Examining the impact of heterogeneous nitryl chloride production on air quality across the United States, Atmospheric Chemistry and Physics, 12, 6455-6473, 10.5194/acp-12-6455-2012, 2012.

Schwartz, C. S., Liu, Z., Lin, H.-C., and Cetola, J. D.: Assimilating aerosol observations with a "hybrid" variational-ensemble data assimilation system, Journal Of Geophysical Research-Atmospheres, 119, 4043-4069, 10.1002/2013jd020937, 2014.

Sekiyama, T. T., Tanaka, T. Y., Shimizu, A., and Miyoshi, T.: Data assimilation of CALIPSO aerosol observations, Atmospheric Chemistry and Physics, 10, 39-49, 10.5194/acp-10-39-2010, 2010.

Shen, Y., Jiang, F., Feng, S., Zheng, Y., Cai, Z., and Lyu, X.: Impact of weather and emission changes on NO2 concentrations in China during 2014–2019, Environmental Pollution, 269, 116163, 10.1016/j.envpol.2020.116163, 2021.

Shi, X. and Brasseur, G. P.: The Response in Air Quality to the Reduction of Chinese Economic Activities During the COVID-19 Outbreak, 47, e2020GL088070, 10.1029/2020gl088070, 2020.

Stavrakou, T., Müller, J.-F., Boersma, K. F., De Smedt, I., and van der A, R. J.: Assessing the distribution and growth rates of NOx emission sources by inverting a 10-year record of NO2 satellite columns, 35, 10.1029/2008gl033521, 2008.

Sun, A. Y., Morris, A., and Mohanty, S.: Comparison of deterministic ensemble Kalman filters for assimilating hydrogeological data, Advances in Water Resources, 32, 280-292, 10.1016/j.advwatres.2008.11.006, 2009.

Takagi, H., Saeki, T., Oda, T., Saito, M., Valsala, V., Belikov, D., Saito, R., Yoshida, Y., Morino, I., Uchino, O., Andres, R. J., Yokota, T., and Maksyutov, S.: On the Benefit of GOSAT Observations to the Estimation of Regional CO_2 Fluxes, SOLA, 7, 161-164, 10.2151/sola.2011-041, 2011.

Tang, X., Zhu, J., Wang, Z. F., and Gbaguidi, A.: Improvement of ozone forecast over Beijing based on ensemble Kalman filter with simultaneous adjustment of initial conditions and emissions,

1119   Atmospheric Chemistry And Physics, 11, 12901-12916, 10.5194/acp-11-12901-2011, 2011.

1120 Tang, X., Zhu, J., Wang, Z. F., Wang, M., Gbaguidi, A., Li, J., Shao, M., Tang, G. Q., and Ji, D. S.:
1121   Inversion of CO emissions over Beijing and its surrounding areas with ensemble Kalman filter,
1122   Atmospheric Environment, 81, 676-686, 10.1016/j.atmosenv.2013.08.051, 2013.

1123 Wang, C., Lei, L., Tan, Z.-M., and Chu, K.: Adaptive Localization for Tropical Cyclones With
1124   Satellite Radiances in an Ensemble Kalman Filter, Frontiers in Earth Science, 8,
1125   10.3389/feart.2020.00039, 2020.

1126 Whitaker, J. S. and Hamill, T. M.: Ensemble data assimilation without perturbed observations,
1127   Monthly   Weather   Review,   130,   1913-1924,   10.1175/1520-
1128   0493(2002)130<1913:Edawpo>2.0.Co;2, 2002.

1129 Wu, H., Tang, X., Wang, Z., Wu, L., Li, J., Wang, W., Yang, W., and Zhu, J.: High-spatiotemporal-
1130   resolution inverse estimation of CO and NOx emission reductions during emission control periods
1131   with a modified ensemble Kalman filter, Atmospheric Environment, 236,
1132   10.1016/j.atmosenv.2020.117631, 2020.

1133 Wu, W. S., Purser, R. J., and Parrish, D. F.: Three-dimensional variational analysis with spatially
1134   inhomogeneous covariances, Monthly Weather Review, 130, 2905-2916, 10.1175/1520-
1135   0493(2002)130<2905:tdvaws>2.0.co;2, 2002.

1136 Zhang, F., Weng, Y., Sippel, J. A., Meng, Z., and Bishop, C. H.: Cloud-Resolving Hurricane
1137   Initialization and Prediction through Assimilation of Doppler Radar Observations with an
1138   Ensemble Kalman Filter, Monthly Weather Review, 137, 2105-2125, 10.1175/2009mwr2645.1,
1139   2009a.

1140 Zhang, Q., Streets, D. G., Carmichael, G. R., He, K. B., Huo, H., Kannari, A., Klimont, Z., Park, I.
1141   S., Reddy, S., Fu, J. S., Chen, D., Duan, L., Lei, Y., Wang, L. T., and Yao, Z. L.: Asian emissions
1142   in 2006 for the NASA INTEX-B mission, Atmospheric Chemistry and Physics, 9, 5131-5153,
1143   10.5194/acp-9-5131-2009, 2009b.

1144 Zhang, S., Zheng, X., Chen, J. M., Chen, Z., Dan, B., Yi, X., Wang, L., and Wu, G.: A global carbon
1145   assimilation system using a modified ensemble Kalman filter, Geosci. Model Dev., 8, 805-816,
1146   10.5194/gmd-8-805-2015, 2015.

1147 Zhang, X., Liu, J., Han, H., Zhang, Y., Jiang, Z., Wang, H., Meng, L., Li, Y. C., and Liu, Y.: Satellite-
1148   Observed Variations and Trends in Carbon Monoxide over Asia and Their Sensitivities to Biomass
1149   Burning, Remote Sensing, 12, 10.3390/rs12050830, 2020.

1150 Zheng, B., Tong, D., Li, M., Liu, F., Hong, C., Geng, G., Li, H., Li, X., Peng, L., Qi, J., Yan, L.,
1151   Zhang, Y., Zhao, H., Zheng, Y., He, K., and Zhang, Q.: Trends in China's anthropogenic emissions
1152   since 2010 as the consequence of clean air actions, Atmospheric Chemistry And Physics, 18,
1153   14095-14111, 10.5194/acp-18-14095-2018, 2018.